

© 2022 IEEE. Personal use of this material is permitted. Permission from IEEE must be obtained for all other uses, in any current or future media, including reprinting/republishing this material for advertising or promotional purposes, creating new collective works, for resale or redistribution to servers or lists, or reuse of any copyrighted component of this work in other works.

J. Chen and C. -I. Chang, "Background Annihilated Target-Constrained Interference-Minimized Filter (TCIMF) for Hyperspectral Target Detection," in *IEEE Transactions on Geoscience and Remote Sensing*, 2022, doi: 10.1109/TGRS.2022.3208519.

<https://doi.org/10.1109/TGRS.2022.3208519>

Access to this work was provided by the University of Maryland, Baltimore County (UMBC) ScholarWorks@UMBC digital repository on the Maryland Shared Open Access (MD-SOAR) platform.

Please provide feedback

Please support the ScholarWorks@UMBC repository by emailing scholarworks-group@umbc.edu and telling us what having access to this work means to you and why it's important to you. Thank you.

Background Annihilated Target-Constrained Interference-Minimized Filter (TCIMF) for Hyperspectral Target Detection

Jie Chen and Chein-I Chang, *Life Fellow, IEEE*

Abstract—Target-constrained interference-minimized filter (TCIMF) has been widely used in various target detection applications for hyperspectral data exploitation. However, like other classic target detection algorithms, the complex background (BKG) of a scene significantly impacts its performance. To better cope with BKG this paper develops a BKG-annihilated TCIMF (BA-TCIMF) which can be implemented in two stages with BKG annihilation in the first stage followed by target detectability enhancement and target BKG suppression performed by TCIMF in the second stage. In particular, the second stage extracts additional BKG signatures from the BKG-annihilated data as unwanted signatures to enhance target detectability via orthogonal subspace projection (OSP), while suppressing target BKG in the BKG-annihilated data by constrained energy minimization (CEM). Depending upon how these two stages are carried out, three versions of BA-TCIMF, data sphered BA-TCIMF (DS-BA-TCIMF), low rank and sparse matrix decomposition (LRaSMD) BA-TCIMF (LRaSMD-BA-TCIMF) and component decomposition analysis-BA-TCIMF (CDA-BA-TCIMF) are derived. Experimental results demonstrate that BA-TCIMF performs as it is designed and better than many existing target detection algorithms.

Index Terms—Background (BKG), BKG-annihilated (BA), Constrained energy minimization (CEM), go decomposition (GoDec), low-rank and sparse matrix decomposition (LRaSMD), target constrained interference-minimized filter (TCIMF).

List of Acronyms

2OS	second order statistics
AUC	area under an ROC curve
BA	BKG-Annihilated
BKG	background
BS	BKG suppression
CEM	constrained energy minimization
CDA	component decomposition analysis
CRD	collaborative representation detector
DS	data sphering
ECEM	ensemble cascaded CEM
GoDec	go decomposition
HCEM	hierarchical CEM

IC	independent component
KTCIMF	kernel TCIMF
LRaSMD	low rank and sparse matrix decomposition
LRR	low rank representation
LSDM	low-rank and sparse decomposition model
MXSVD	minimax singular value decomposition
ODP	overall detection probability
OSP	orthogonal subspace projection
PC	Principal component
ROC	receiver operating characteristic
SNPR	signal-to-noise probability ratio
TBS	target background suppression
TDE	target detectability enhancement
TD	target detectability
TCIMF	target constrained interference-minimized filter
VD	virtual dimensionality

I. INTRODUCTION

HYPERSPECTRAL imagery is a data cube which is acquired by three dimensions, two spatial dimensions and one spectral dimension. Thus, every pixel is indeed a vector of which each component corresponds to the measurement of a spectral value acquired by a specific spectral wavelength [1–4]. The very fine spectral resolution provided by hundreds of contiguous spectral bands allows a hyperspectral imager to uncover and reveal many subtle material substances which cannot be identified by prior knowledge or visual inspection in many applications, specifically, subpixel detection, anomaly detection, endmember finding, mixed pixel classification and quantification, etc.

Over last decades, a variety of target detection methods have been developed. For example, Harsanyi and Chang [1,5–6] developed a target detection approach from a mixed signal detection which annihilated undesired signals by orthogonal subspace projection (OSP) before target detection takes place. Technically speaking, the key success for OSP is its use of orthogonal subspace projector, P_U^\perp , which annihilates the signal sources specified by an undesired target signature matrix U . However, it is very sensitive to the knowledge of U . Since many unknown signals cannot be known *a priori* to be included in the U , this limits the utilization of OSP. To mitigate this dilemma, Harsanyi first developed a constrained energy minimization (CEM) approach in his dissertation [7] and latter in an application [8]. It constrained the target to be detected while suppressing all other signal sources by inverting the sample correlation matrix to enhance target detection with more details provided in [9]. By taking advantage of OSP and CEM, Ren and Chang in [10] combined OSP and CEM to derive target-constrained interference-

Manuscript received May 20, 2022; revised August 22, 2022; accepted September 16, 2022. (Corresponding author: Chein-I Chang)

J. Chen is with Remote Sensing Signal and Image Processing Laboratory, Department of Computer Science and Electrical Engineering, University of Maryland, Baltimore County, Baltimore, MD 21250 USA. (e-mail: jchen18@umbc.edu).

C.-I Chang is with Information and Technology College, Dalian Maritime University, Dalian, China and Remote Sensing Signal and Image Processing Laboratory, Department of Computer Science and Electrical Engineering, University of Maryland, Baltimore County, Baltimore, MD 21250 USA, Department of Computer Science and Information Management, Providence University, Taichung 02912, Taiwan, ROC. (e-mail: cchang@umbc.edu).

minimized filter (TCIMF) which used OSP to annihilate undesired targets to increase target detectability and in the meantime used CEM to improve target background suppression (TBS) simultaneously. All these three algorithms are included in the popular software ENVI (Environment for Visualizing Images) which is developed by L3Harris Geospatial and has been widely used for remote sensing image analysis [11].

One major strength of TCIMF is its ability in remedying the deficiency of OSP by including the strength of CEM which suppresses unknown BKG via inverting the sample correlation matrix. Nevertheless, TCIMF still has two inherent issues arising from the undesired signature matrix \mathbf{U} which must be known *a priori* like OSP. In many real-world applications, this assumption is not practical due to the fact that hyperspectral imaging can uncover many unknown signal sources which cannot be identified by prior knowledge, specifically, BKG. A second issue is that TCIMF is also very sensitive to the knowledge of \mathbf{U} . If the \mathbf{U} is provided precisely, TCIMF works very effectively. On the other hand, if \mathbf{U} is not reliable, then TCIMF may not perform as well as it is designed. To further alleviate this problem, TCIMF was subsequently extended by a signal decomposition interference annihilated (SDIA) approach [12] which used a signal decomposition interference noise (SDIN) model to generate a set of unknown interfering signature sources specified by Ψ that can be found by automatic target generation process (ATGP) [13]. Using Ψ as additional interfering signal sources in conjunction with \mathbf{U} , TCIMF improves its detection performance for better interference annihilation. Unfortunately, with significantly improved spatial and spectral resolution a hyperspectral image scene becomes more complicated than a multispectral image scene. The ATGP-generated interfering signal sources Ψ used by the SDIN model may not be capable of taking care of the BKG issue effectively if Ψ is unable to faithfully represent BKG signatures.

In order to deal with BKG more effectively, we look closely into the structure of TCIMF which is actually designed to tackle two types of BKG. One is the global BKG which can be suppressed by inverting \mathbf{R} via CEM. The other is target BKG, which can be suppressed by annihilating \mathbf{U} via OSP. The SDIA proposed in [12] extended TCIMF by introducing interfering signal sources Ψ as unwanted signal sources to be annihilated by OSP so as to enhance target detection. However, both TCIMF and SDIA did not look into the issue in how to effectively suppress the global BKG. This paper investigates these two types of BKG and generalizes TCIMF from a rather different perspective.

To annihilate the global BKG, three approaches are of particular interest. One is to assume that BKG can be characterized by the first two orders of data statistics (2OS). In this case, data sphering (DS) [2, chapter 6] is then applied to annihilate BKG prior to target detection. This DS was further used to expand OSP's capability in improving target detection [14] and anomaly detection [15]. A second one is to represent a data space \mathbf{X} as a decomposition of a low rank subspace \mathbf{L} and sparse subspace \mathbf{S} so that \mathbf{L} and \mathbf{S} can be used to specify the BKG and target spaces, respectively. One of most studied techniques in recent years is the low rank and sparse matrix

decomposition (LRaSMD) proposed in [16] which decomposes a data space \mathbf{X} as a three-component space, low rank space \mathbf{L} , sparse space \mathbf{S} and noise space \mathbf{N} . Unlike LRaSMD, a third approach was recently developed by Chen et al. in [17], called component decomposition analysis (CDA) which decomposed a data space into principal component (PC), independent component (IC) and noise component.

In this paper, we integrate the above three individual approaches into TCIMF to derive BKG annihilated TCIMF (BA-TCIMF) to yield the global BKG-annihilated data space, \mathbf{X}_{BA} . We then use an unsupervised method to generate unwanted BKG signatures from \mathbf{X}_{BA} for TBS so as to improve target detectability. In essence, BA-TCIMF makes use of two pre-processing steps to deal with two types of BKG issues, global BKG annihilation and target BKG annihilation prior to TCIMF for target detection.

In order to further explore nonlinear structures of TCIMF a kernel version of TCIMF, kernel TCIMF (KTCIMF) was generalized in [18] and can be used to extend BA-TCIMF to derive BA-KTCIMF. Unfortunately, due to the fact that TCIMF already significantly improves its detection performance, the advantages offered by KTCIMF will be limited. Accordingly, the benefits gained by KTCIMF are not well-paid off at the expense of its exceedingly high computational complexity, which will be shown in the experiments conducted in this paper. Nevertheless, BA-KTCIMF can still manage to improve KTCIMF.

It has been shown in [19] that the commonly used two-dimensional receiver operating characteristics (2D ROC) curve of detection probability P_D versus false alarm probability P_F was ineffective because both P_D and P_F are determined by the same threshold and cannot stand alone to be used as independent criteria. Specifically, when P_D is high, P_F is also high and vice versa. Consequently, using the area under the curve (AUC) of the 2D ROC curve of (P_D, P_F) cannot be used to evaluate BS. In particular, Chang in [19] introduced a 3D ROC curve from which three 2D ROC curves can be derived, i.e., 2D ROC curve of (P_D, P_F) , 2D ROC curve of (P_D, τ) , 2D ROC curve of (P_F, τ) . Based on these three 3D ROC curve-derived 2D ROC curves, eight detection measures were designed to evaluate AD performance in terms of TD, BS, joint TD and BS (TDBS) and overall detection performance (ODP).

Several novelties are summarized below.

1. It introduces new concept of BA into TCIMF to derive BA-TCIMF, which can accomplish global BKG annihilation and target BKG annihilation.
2. It uses DS, LRaSMD and CDA to accomplish the global BKG annihilation.
3. It further implements an unsupervised means to find unwanted BKG signatures for TBS.
4. It allows BA-TCIMF to detect targets and suppress BKG in different spaces.
5. It does not need training samples to achieve BA as many deep learning (DL) or model-based works reported in the literature.

The above novelties yield following main contributions.

1. It generalizes TCIMF to BA-TCIMF in two stage processes with the first stage for global BKG annihilation

- followed by the 2nd stage to perform TDE and TBS.
2. It derives three versions of BA-TCIMF, DS-BA-TCIMF, LRSMD-BA-TCIMF and CDA-BA-TCIMF.
 3. It also uses MXSVD to extract BKG signatures from the low rank space \mathbf{L} for DS-BA-TCIMF, LRSMD-BA-TCIMF and CDA-BA-TCIMF as additional unknown BKG signatures so as to achieve better TDE and TBS.
 4. Finally, it extends BA-TCIMF to training sampling-based BA-TCIMF to study the robustness of TCIMF to its training samples-calculated target signature matrix \mathbf{D} .

The remainder of this paper is organized as follows. Section II briefly reviews related works. Section III derives BA-TCIMF which has three versions of BA-TCIMF, DS-BA-TCIMF, LRSMD-BA-TCIMF and CDA-BA-TCIMF. Section IV describes the data sets to be studied along with 3D ROC curve derived detection measures to address the BKG issue in target detection. Section V performs extensive experiments and discusses their results. Section VI extends BA-TCIMF to training sampling-based BA-TCIMF and BA-KTCIMF. Section VII summarizes conclusions.

II. RELATED WORKS

Target detection has been studied extensively and comprehensively in [20] where various target detectors have derived. Among them CEM and OSP are two of most promising target detectors where many variants were also derived such as SDIA in [12], ATGP in [13], OSP-TD in [14], linearly constrained minimum variance (LCMV) in [9], TCIMF [10], hierarchical CEM (HCEM) [21], ensemble cascaded CEM (ECEM) [22], CEM anomaly detector (CEMAD) [23], kernel CEM (KCEM) [24]. Interestingly, TCIMF is the only one which combines the strengths of both OSP and CEM and is the main base detector to derive BA-TCIMF in this paper.

A. Target Constrained Interference Minimize Filter

Comparing to Orthogonal subspace projection (OSP) [6], the main strength of CEM [7] is to pass the desired signal while minimizing output energy of unknown signal sources without obtaining them. However, TCIMF [10] needs the undesired signal as a prior, which limited its application in the practices because the undesired signals usually include the unknown signal sources that are almost impossible to be acquired. In target detection applications, signal sources can be divided into two categories, one of them is targets of interest as the desired targets, and the targets of no interest as unwanted targets such as undesired signal sources by prior knowledge. Naturally, eliminating or suppressing these unwanted signal sources will lead to an increase in the detectability of targets of interest. To achieve this goal, the idea of the TCIMF can be described as the following procedure. Let the known signals were decomposed into interesting signals, \mathbf{D} , denoted by $\mathbf{D}=[\mathbf{d}_1\mathbf{d}_2\ldots\mathbf{d}_p]$ and uninteresting signals, \mathbf{U} , denoted by $\mathbf{U}=[\mathbf{u}_1\mathbf{u}_2\ldots\mathbf{u}_q]$ as an

undesired target signature matrix. Now, if we let $\mathbf{c}=\begin{bmatrix} \mathbf{1}_{p\times 1} \\ \mathbf{0}_{q\times 1} \end{bmatrix}$

constrain these two target matrices by

$$(\mathbf{DU})^T \mathbf{w} = \begin{bmatrix} \mathbf{1}_{p\times 1} \\ \mathbf{0}_{q\times 1} \end{bmatrix} = \begin{bmatrix} \underbrace{1, \dots, 1}_p, \underbrace{0, \dots, 0}_q \end{bmatrix}^T \quad (1)$$

where $\mathbf{DU}=[\mathbf{d}_1\mathbf{d}_2\ldots\mathbf{d}_p\mathbf{u}_1\mathbf{u}_2\ldots\mathbf{u}_q]$ and $\mathbf{1}_{p\times 1}$ is a $p\times 1$ vector with ones in all components and $\mathbf{0}_{q\times 1}$ is a $q\times 1$ vector with zero in its components, where 1 represents the desired targets and 0 represents the undesired targets. Using (14) as a constraint vector, TCIMF can be formulated as the following multi-desired targets-constrained and multi-undesired targets-annihilated optimization problem:

$$\min_{\mathbf{w}} \{ \mathbf{w}^T \mathbf{R} \mathbf{w} \} \text{ subject to } (\mathbf{DU})^T \mathbf{w} = \begin{bmatrix} \mathbf{1}_{p\times 1} \\ \mathbf{0}_{q\times 1} \end{bmatrix} \quad (2)$$

where \mathbf{R} is the global correlation matrix and the optimal weight vector \mathbf{w}^* can be obtained by

$$\mathbf{w}^* = \mathbf{R}^{-1} \mathbf{DU} \left((\mathbf{DU})^T \mathbf{R}^{-1} \mathbf{DU} \right)^{-1} \begin{bmatrix} \mathbf{1}_{p\times 1} \\ \mathbf{0}_{q\times 1} \end{bmatrix}. \quad (3)$$

The FIR filter coefficient specified by \mathbf{w}^* given above is called the TCIMF given by

$$\delta^{\text{TCIMF}}(\mathbf{r}) = \left(\mathbf{R}^{-1} \mathbf{DU} \left((\mathbf{DU})^T \mathbf{R}^{-1} \mathbf{DU} \right)^{-1} \begin{bmatrix} \mathbf{1}_{p\times 1} \\ \mathbf{0}_{q\times 1} \end{bmatrix} \right)^T \mathbf{r} \quad (4)$$

with $\mathbf{w}^{\text{TCIMF}} = \mathbf{w}^*$ specified by (3). Now if we assume that \mathbf{d} is a desired target signature and let $\mathbf{D}=\mathbf{d}$ and $\mathbf{U}=\emptyset$, then (2) is reduced to

$$\min_{\mathbf{w}} \{ \mathbf{w}^T \mathbf{R} \mathbf{w} \} \text{ subject to } \mathbf{d}^T \mathbf{w} = 1 \quad (5)$$

which yields the CEM subpixel target detector derived in [7],

$$\delta^{\text{CEM}}(\mathbf{r}) = \frac{\mathbf{d}^T \mathbf{R}^{-1} \mathbf{r}}{(\mathbf{d}^T \mathbf{R}^{-1} \mathbf{d})} \quad (6)$$

On the other hand, if we assume that \mathbf{d} is a desired target signature and let $\mathbf{D}=\mathbf{d}$, $\mathbf{U}=\emptyset$ and $\mathbf{R}^{-1}=P_U^\perp$, then (2) is reduced to OSP-TD,

$$\delta^{\text{OSP}}(\mathbf{r}) = \frac{\mathbf{d}^T P_U^\perp \mathbf{r}}{(\mathbf{d}^T P_U^\perp \mathbf{d})} \quad (7)$$

where P_U^\perp is OSP annihilation projection matrix given by

$$P_U^\perp = \mathbf{I} - \mathbf{U}(\mathbf{U}^T \mathbf{U})^{-1} \mathbf{U}^T \quad (8)$$

It is equivalent to replacing \mathbf{R}^{-1} in (6) with P_U^\perp .

B. Matrix Decomposition for Global BKG Annihilation

To annihilate the global BKG, three approaches are of particular interest.

1) DS

It assumes that global BKG can be characterized by the first two orders of data statistics (2OS), mean $\boldsymbol{\mu}$ and covariance matrix \mathbf{K} . The data sphering (DS) is performed by mapping the original data sample vector \mathbf{r} to its sphered data sample vector $\hat{\mathbf{r}}$ in the sphered data space $\hat{\mathbf{X}}$ by

$$\hat{\mathbf{r}} = \mathbf{K}^{-1/2} (\mathbf{r} - \boldsymbol{\mu}) \quad (9)$$

where $\mathbf{K}^{-1/2}$ is referred to as whitening matrix in [26]. Details of DS can be found in [2, section 6.3.1] along with its code [2, pp. 1000-1001]. It is interesting to see that the well-known anomaly detector developed by Reed and Xiaoli, RXD in [25] is given by

$$\delta^{\text{RXD}}(\mathbf{r}) = (\mathbf{r} - \boldsymbol{\mu})^T \mathbf{K}^{-1} (\mathbf{r} - \boldsymbol{\mu}) \quad (10)$$

which happens to be the Mahalanobis distance between \mathbf{r} and $\boldsymbol{\mu}$. Now, if we re-write \mathbf{K}^{-1} as $\mathbf{K}^{-1} = \mathbf{K}^{-1/2} \mathbf{K}^{-1/2}$, then using (9) (10) can be re-expressed

$$(\mathbf{K}^{-1/2} (\mathbf{r} - \boldsymbol{\mu}))^T \mathbf{K}^{-1/2} (\mathbf{r} - \boldsymbol{\mu}) = \|\mathbf{K}^{-1/2} (\mathbf{r} - \boldsymbol{\mu})\|^2 = \|\hat{\mathbf{r}}\|^2 \quad (11)$$

which turns out to be the vector length of $\hat{\mathbf{r}}$. This shows that for each data sample vector \mathbf{r} , RXD is nothing more than finding the vector length of its sphered data sample vector $\hat{\mathbf{r}}$.

2) Matrix Decomposition

Another is to represent a data space \mathbf{X} as a decomposition of a low rank subspace \mathbf{L} and sparse subspace \mathbf{S} so that \mathbf{L} and \mathbf{S} can be used to specify the BKG and target spaces, respectively. This approach has been one of most studied techniques in recent years.

a) RPCA

One earlier approach was robust principal component analysis (RPCA) developed by Candes *et al.* in [27] which decomposed the data matrix \mathbf{X} into a matrix decomposition

$$\mathbf{X} = \mathbf{L} + \mathbf{S} \quad (12)$$

where \mathbf{L} is a low-rank matrix and \mathbf{S} has an arbitrary magnitude where the given data \mathbf{X} is assumed to be of low inherent dimensionality. RPCA can cope with the noise of extremely high amplitude by principal component pursuit (PCP) estimate which solves

$$\text{minimize } \|\mathbf{L}\|_* + \lambda \|\mathbf{S}\|_1 \text{ subject to } \mathbf{L} + \mathbf{S} = \mathbf{X} \quad (13)$$

where $\|\mathbf{L}\|_*$ is defined by the nuclear norm.

Interestingly, Vaswani *et al.* developed an approach in [28-29], called robust subspace learning (RSL) which treated an outlier as an additive sparse corruption via sparse+low-rank (S+LR) matrix decomposition. Using this interpretation, RPCA can be considered as a variant of RSL via S+LR formulation.

b) LRSMD

One major problem with (12) is that noise and sparse signals are blended in \mathbf{S} . As a result, on one end, noise may mistakenly for targets which result in false alarms. On another end, targets may be treated as noise which causes missing targets. Either case will degrade detection performance. To resolve this issue, a more attractive model, called the low rank and sparse matrix decomposition (LRSMD) was proposed in [16] which decomposes a data space \mathbf{X} as a three-component space,

$$\mathbf{X} = \mathbf{L} + \mathbf{S} + \mathbf{N} \quad (14)$$

where an algorithm, called go decomposition (GoDec) was designed to produce the low rank space \mathbf{L} , sparse space \mathbf{S} and noise space \mathbf{N} . Recently, GoDec was further extended to OSP-GoDec in [30]. As a result of (14), OSP can be operated on the low rank space \mathbf{L} via an OSP annihilator P_L^\perp can be obtained from (8) by replacing \mathbf{U} with \mathbf{L} as

$$\mathbf{X}_L^\perp = P_L^\perp \mathbf{X} \quad (15)$$

for BKG annihilation which maps \mathbf{X} onto the space \mathbf{X}_L^\perp orthogonal to the low-rank space \mathbf{L} to annihilate \mathbf{L} which is considered as the BKG space.

b) CDA

A third approach is recently developed by Chen *et al.* in [17], called component decomposition analysis (CDA) which represents a data space as a decomposition of principal component (PC), independent component (IC) and noise component spaces by

$$\mathbf{X} = \mathbf{PC} + \mathbf{IC} + \mathbf{N}. \quad (16)$$

By assuming that BKG is characterized by the principal component space, \mathbf{PC} , BKG annihilation can be accomplished by

$$\mathbf{X}_{\mathbf{PC}}^\perp = P_{\mathbf{PC}}^\perp \mathbf{X} = (\mathbf{I} - P_{\mathbf{PC}}) \mathbf{X} \quad (17)$$

$$\text{with } P_{\mathbf{PC}} = \mathbf{PC} (\mathbf{PC}^T \mathbf{PC})^{-1} (\mathbf{PC}^T)^T.$$

C. GoDec

Inspired by matrix decomposition and RPCA, GoDec develops its theory to manipulate the low-rank approximation and sparse presentation. It firstly projects an input dense matrix on its columns space, $\mathbf{Y}_1 = \mathbf{X} \mathbf{A}_1$ and then its rows space, $\mathbf{Y}_2 = \mathbf{X}^T \mathbf{A}_2$, respectively, where \mathbf{A}_1 , \mathbf{A}_2 are random matrices. The projection process is a so-called bilateral random projection (BRP). This process is similar to Halko's randomized approximate matrix decomposition [31] except for the number of projections. So, the low-rank matrix is given by

$$\mathbf{L} = \mathbf{Y}_1 (\mathbf{A}_2 \mathbf{Y}_1)^{-1} \mathbf{Y}_2 \quad (18)$$

After obtaining the low-rank approximation, GoDec uses the model,

$$\mathbf{X} = \mathbf{L} + \mathbf{S} + \mathbf{N} \text{ subject to } \text{rank}(\mathbf{L}) \leq r, \text{card}(\mathbf{S}) \leq k \quad (19)$$

where $\text{card}(\mathbf{S})$ is defined as sparsity cardinality (SC) of \mathbf{S} . Recall that RPCA also uses the $\mathbf{X} = \mathbf{L} + \mathbf{S}$ in a similar manner. But the difference is that \mathbf{S} in (19) contains only sparse signals, whereas \mathbf{S} in RPCA is a noise matrix.

As noted above, both the randomized power iteration algorithm [31] and GoDec [16] provide a means of overcoming the singular values with slow decay operating on $\tilde{\mathbf{X}} = (\mathbf{X} \mathbf{X}^T)^\gamma \mathbf{X}$ rather than the original input matrix \mathbf{X} . In a randomized power iteration algorithm, it uses $\tilde{\mathbf{X}}$ to perform random sampling and then to obtain the sampling matrix. On the other hand, GoDec uses BRP to solve the following low-rank approximation

$$\mathbf{L} = \mathbf{Q}_1 \left[\mathbf{R}_1 (\mathbf{A}_2^T \mathbf{Y}_1)^{-1} \mathbf{R}_2^T \right]^{1/(2\gamma+1)} \mathbf{Q}_2^T \quad (20)$$

where $\mathbf{Q}_1, \mathbf{Q}_2, \mathbf{R}_1, \mathbf{R}_2$ are QR decomposition of $\mathbf{Y}_1, \mathbf{Y}_2$. In addition, the model in (19) can be further solved by minimizing the following decomposition error

$$\min_{\mathbf{L}_{N \times L}, \mathbf{S}_{N \times L}} \|\mathbf{X}_{N \times L} - \mathbf{L}_{N \times L} - \mathbf{S}_{N \times L}\|_F^2$$

$$\text{subject to } \text{rank}(\mathbf{L}_{N \times L}) \leq r \text{ and } \text{cardinality}(\mathbf{S}_{N \times L}) \leq jN \quad (21)$$

where $\|\cdot\|_F$ is the Frobenius matrix norm. Since (21) does not have an analytical solution, it must rely on a numerical algorithm, which is GoDec to find solutions by the following iterative processes.

$$\begin{aligned}\mathbf{L}_{N \times L}^{(t)} &= \arg \min_{\text{rank}(\mathbf{L}_{N \times L}) \leq r} \|\mathbf{X}_{N \times L} - \mathbf{L}_{N \times L} - \mathbf{S}_{N \times L}^{(t-1)}\|_F^2 \\ \mathbf{S}_{N \times L}^{(t)} &= \arg \min_{\text{cardinality}(\mathbf{S}_{N \times L}) \leq jN} \|\mathbf{X}_{N \times L} - \mathbf{L}_{N \times L}^{(t-1)} - \mathbf{S}_{N \times L}\|_F^2\end{aligned}\quad (22)$$

The details of implementing GoDec are summarized as follows.

<i>GoDec</i>	
Input:	$\mathbf{X}_{N \times L}$ input data matrix
	r : the rank of the low rank matrix \mathbf{L}
	k : sparsity cardinality for sparsity matrix \mathbf{S}
	ε : pre-determined the error
	γ : power scheme
Output:	
	$\mathbf{L}_{N \times L}$: Low rank matrix
	$\mathbf{S}_{N \times L}$: Sparsity matrix
<hr/>	
Initialize:	$\mathbf{L}_{N \times L}^{(0)} = \mathbf{X}_{N \times L}, \mathbf{S}_{N \times L}^{(0)} = \mathbf{O}_{N \times L}, t = 0$
While	$\ \mathbf{X}_{N \times L} - \mathbf{L}_{N \times L} - \mathbf{S}_{N \times L}^{(t-1)}\ _F^2 / \ \mathbf{X}_{N \times L}\ _F^2 > \varepsilon$ Do
	$t = t + 1;$
	$\tilde{\mathbf{L}} = [(\mathbf{X}_{N \times L} - \mathbf{S}_{N \times L}^{t-1})(\mathbf{X}_{N \times L} - \mathbf{S}_{N \times L}^{t-1})^T]^\gamma (\mathbf{X}_{N \times L} - \mathbf{S}_{N \times L}^{t-1})$
	$\mathbf{Y}_1 = \tilde{\mathbf{L}}\mathbf{A}_1, \mathbf{A}_2 = \mathbf{Y}_1;$
	$\mathbf{Y}_2 = (\tilde{\mathbf{L}})^T \mathbf{Y}_1 = \mathbf{Q}_2 \mathbf{R}_2, \mathbf{Y}_1 = \tilde{\mathbf{L}} \mathbf{Y}_2 = \mathbf{Q}_1 \mathbf{R}_1;$
	$\mathbf{L}_{N \times L}^{(t)} = \mathbf{Q}_1 [\mathbf{R}_1 (\mathbf{A}_2^T \mathbf{Y}_1)^{-1} \mathbf{R}_2^T]^{1/(2\gamma+1)} \mathbf{Q}_2^T;$
	$\mathbf{S}_{N \times L}^{(t)} = P_\Omega(\mathbf{X}_{N \times L} - \mathbf{L}_{N \times L}^{(t)})$ (23)
	where Ω is the nonzero subset of the first k largest entries of
	$ \mathbf{X}_{N \times L} - \mathbf{L}_{N \times L}^{(t)} ;$
End While	

It should be noted that the four parameters, $r, k, \varepsilon, \gamma$ in the above algorithm must be determined in advance as initial conditions. Since there are no guidelines provided in [16], these parameters have been selected empirically by experiments. Fortunately, in a recent work [30], Chang *et al.* interpreted and re-derived GoDec as an OSP-based GoDec (OSP-GoDec) which only required determining the parameter k . In particular, this OSP-GoDec took advantage of VD in [1,32-36] and the minimax singular value decomposition (MX-SVD) developed in [37] to automatically determine the value of k . This significant benefit allows GoDec to be implemented without determining all the four parameters, $r, k, \varepsilon, \gamma$ empirically. So, it makes GoDec more accessible and increase its utilization in many future works to come [14-15]. The reason that GoDec was used in this is simply because GoDec is widely used in the literature and the details along with its implementations are available on the website¹. In this case, those who are interested in BA-TCIMF can easily adapt and implement BA-TCIMF for experiments. Nevertheless, OSP-GoDec can be also used as an alternative to GoDec.

A final remark on the projection P_Ω used in (23) is noteworthy. It was derived from video anomaly detection in [16] where SC is specified by a predetermined value k and the space Ω is the set of retaining the k largest nonzero elements

in the sparse space \mathbf{S} generated by GoDec. The $\mathbf{S}_{N \times L}^{(t)}$ in (23) is simply the space Ω obtained by mapping from $\mathbf{X}_{N \times L} - \mathbf{L}_{N \times L}^{(t-1)}$ onto Ω via the projection P_Ω . For various comparative analyses can be found in references [14-15,17,30,38], specifically, reference [38]. Those who are interested in Scare encouraged to consult [17,38] for more details of SC interpretations and derivations. In particular, Chang in [38] provided how the concept of SC was derived and also offered different versions of SC.

III. BA-TCIMF

This section presents key ideas that are used to develop BA-TCIMF. Basically, BA-TCIMF can be implemented in two successive stages with the global BKG annihilated in the first stage followed by TBS carried out in the second stage.

A. Global BKG Annihilation

According to the above three approaches, DS, LRA-SMD and CDA described in Section II three versions of BA-TCIMF, DS-BA-TCIMF, LRA-SMD-BA-TCIMF and CDA-BA-TCIMF can be derived, each of which is described in detail in as separate subsection.

• First stage for BKG Annihilation:

- DS-BA-TCIMF spheres data by removing 2OS. The resulting data space is denoted by $\hat{\mathbf{X}} = \mathbf{X}_{\text{DS}}$.
- LRA-SMD-BA-TCIMF uses the GoDec-produced low rank space \mathbf{L} as \mathbf{U} and then annihilates BKG via $P_{\mathbf{L}}^\perp$ in (2). The resultant space is denoted by $\mathbf{X}_{\mathbf{L}}^\perp$.
- CDA-BA-TCIMF implements the CDA model to produce principal component space, \mathbf{PC} and applies $P_{\mathbf{PC}}^\perp$ in (4) to annihilate BKG. The resultant space is denoted by $\mathbf{X}_{\mathbf{PC}}^\perp$.

• Second stage for TDE and TBS:

- DS-BA-TCIMF extracts BKG signatures from the GoDec-produced low rank space $\hat{\mathbf{L}}$ in $\hat{\mathbf{X}} = \mathbf{X}_{\text{DS}}$ which are used as additional unwanted signatures to increase and enhance target detectability. In the meantime, DS-BA-TCIMF also calculates and inverts a sample correlation matrix $\mathbf{R}_{\text{BA}} = \hat{\mathbf{R}}$ in $\hat{\mathbf{X}} = \mathbf{X}_{\text{DS}}$ to improve TBS.
- LRA-SMD-BA-TCIMF extracts m BKG signatures from $\mathbf{X}_{\mathbf{L}}^\perp$ which are further used as additional unwanted signatures to increase and enhance target detectability. At the same time, LRA-SMD-BA-TCIMF also inverts a sample correlation matrix $\mathbf{R}_{\text{BA}} = \mathbf{R}_{\mathbf{L}+\mathbf{S}}$ obtained from the joint $\mathbf{L}+\mathbf{S}$ space to improve TBS.
- CDA-BA-TCIMF extracts m BKG signatures from $\mathbf{X}_{\mathbf{PC}}^\perp$ which are used as additional unwanted signatures to increase and enhance target detectability. Then it also inverts a sample correlation matrix $\mathbf{R}_{\text{BA}} = \mathbf{R}_{\mathbf{PC}+\mathbf{IC}}$ calculated from the joint $\mathbf{PC}+\mathbf{IC}$ space to improve TBS.

¹<https://sites.google.com/site/godecomposition/home>

B. Target BKG Annihilation

After the global BKG annihilation, we further look into TBS. More specifically, we want to enhance target detectability by annihilating additional BKG signatures extracted from the BKG-annihilated data space while inverting the BKG-annihilated correlation matrix, denoted by \mathbf{R}_{BA} to achieve further BKG suppression. In doing so, TCIMF divided targets of interest into desired targets, $\mathbf{d}_1, \mathbf{d}_2, \dots, \mathbf{d}_p$ and undesired targets, $\mathbf{u}_1, \mathbf{u}_2, \dots, \mathbf{u}_q$ embedded in BKG. Since TCIMF is very sensitive to its use of target knowledge via OSP, the contamination of BKG effect on these targets may result in poor detection performance. So, TCIMF can be implemented in two consecutive stages with the first stage to annihilate global BKG prior to acquiring target knowledge and then followed by the second stage to extract \mathbf{D} and \mathbf{U} from this annihilated BKG, denoted by \mathbf{D}_{BA} and \mathbf{U}_{BA} . Apparently, there are also unknown BKG signatures that cannot be identified by visual inspection or prior knowledge and should be included in \mathbf{U}_{BA} for further BKG annihilation to enhance target detectability. In doing so, the singular value decomposition (SVD) can be used for this purpose to extract additional m BKG signatures, $\mathbf{b}_1, \mathbf{b}_2, \dots, \mathbf{b}_m$ to form a BKG signature matrix $\mathbf{B}_m = [\mathbf{b}_1 \mathbf{b}_2 \dots \mathbf{b}_m]$ that can be implemented in conjunction with $\mathbf{D}_{BA} \mathbf{U}_{BA}$ to replace \mathbf{DU} in (1) as $\mathbf{D}_{BA} \mathbf{U}_{BA} \mathbf{B}_m$. Such signature augmentation is similar to the SDIN model used by SDIA but offers better BKG annihilation than SDIA because its knowledge obtained from the annihilated BKG not from the original data space. In the meantime, TCIMF also takes advantage of CEM to suppress target BKG via inverting a correlation matrix of annihilated BKG, \mathbf{R}_{BA} to replace the global \mathbf{R} in (2) to improve target BKG suppression. Accordingly, there are two key processes that improve TCIMF, global BKG annihilation in the first stage followed by the second stage which includes additional BKG signatures to augment the BKG annihilated $\mathbf{D}_{BA} \mathbf{U}_{BA}$ for better BKG annihilation so as to enhance target detectability, while also improving target BKG suppression by using annihilated correlation matrix \mathbf{R}_{BA} . This leads to a new improved two-stage TCIMF, called BA-TCIMF as shown in Fig. 1 where the first stage is to annihilate BKG prior to TCIMF followed by the second stage which performs both TDE and TBS.

Depending upon how to perform global BKG annihilation for BA-TCIMF, three versions of BA-TCIMF can be derived as follows.

1) DS-BA-TCIMF

The first version of BA-TCIMF is to use DS to annihilate the 2OS-characterized global BKG prior to TCIMF. It is then followed by applying GoDec to the sphered data $\hat{\mathbf{X}}$ to yield the sphered LRA-SMD representation given by

$$\hat{\mathbf{X}} = \hat{\mathbf{L}} + \hat{\mathbf{S}} + \hat{\mathbf{N}}. \quad (24)$$

Using $\hat{\mathbf{L}}$ in (18) MXSVD is used to find m BKG signatures $\{\hat{\mathbf{b}}_1, \hat{\mathbf{b}}_2, \dots, \hat{\mathbf{b}}_m\}$ to form a BKG signature matrix $\hat{\mathbf{B}}_{\hat{\mathbf{L}}} = [\hat{\mathbf{b}}_1 \hat{\mathbf{b}}_2 \dots \hat{\mathbf{b}}_m]$, i.e., $\hat{\mathbf{B}}_{\hat{\mathbf{L}}} = \mathbf{B}_m$ in Fig. 2(a). By coupling

with $\hat{\mathbf{D}}\hat{\mathbf{U}} = [\hat{\mathbf{d}}_1 \hat{\mathbf{d}}_2 \dots \hat{\mathbf{d}}_p, \hat{\mathbf{u}}_1 \hat{\mathbf{u}}_2 \dots \hat{\mathbf{u}}_q]$ obtained from the \mathbf{DU} in the sphered data $\hat{\mathbf{X}} = \mathbf{X}_{DS}$ we can augment \mathbf{DU} in (1) to a new target matrix $\hat{\mathbf{D}}\hat{\mathbf{U}}\hat{\mathbf{B}} = [\hat{\mathbf{d}}_1 \hat{\mathbf{d}}_2 \dots \hat{\mathbf{d}}_p, \hat{\mathbf{u}}_1 \hat{\mathbf{u}}_2 \dots \hat{\mathbf{u}}_q, \hat{\mathbf{b}}_1 \hat{\mathbf{b}}_2 \dots \hat{\mathbf{b}}_m]$ to yield a new constraint matrix

$$(\hat{\mathbf{D}}\hat{\mathbf{U}}\hat{\mathbf{B}})^T \hat{\mathbf{w}} = \begin{bmatrix} \mathbf{1}_{p \times 1} \\ \mathbf{0}_{q \times 1} \\ \mathbf{0}_{m \times 1} \end{bmatrix} = \begin{bmatrix} \underbrace{1, \dots, 1}_p, \underbrace{0, \dots, 0}_q, \underbrace{0, \dots, 0}_m \end{bmatrix}^T \quad (25)$$

for further BKG annihilation to enhance target detectability.

In the meantime, the \mathbf{R} in (2) is replaced by $\hat{\mathbf{R}} = \frac{1}{N} \sum_{i=1}^N \hat{\mathbf{r}}_i \hat{\mathbf{r}}_i^T$

which is the correlation matrix formed by data samples in $\hat{\mathbf{X}}$ to further improve target BKG suppression in $\hat{\mathbf{X}}$. By virtue of $\hat{\mathbf{D}}\hat{\mathbf{U}}\hat{\mathbf{B}}$ in (25) and $\hat{\mathbf{R}}$ the constrained optimization problem (2) can be extended to a sphered target-augmented constrained optimization problem given by

$$\min_{\hat{\mathbf{w}}} \{\hat{\mathbf{w}}^T \hat{\mathbf{R}} \hat{\mathbf{w}}\} \text{ subject to } (\hat{\mathbf{D}}\hat{\mathbf{U}}\hat{\mathbf{B}})^T \hat{\mathbf{w}} = \begin{bmatrix} \mathbf{1}_{p \times 1} \\ \mathbf{0}_{q \times 1} \\ \mathbf{0}_{m \times 1} \end{bmatrix} \quad (26)$$

The optimal solution to (26) is the weight vector $(\hat{\mathbf{w}})^*$ given by

$$(\hat{\mathbf{w}})^* = \hat{\mathbf{R}}^{-1} \hat{\mathbf{D}}\hat{\mathbf{U}}\hat{\mathbf{B}} \left((\hat{\mathbf{D}}\hat{\mathbf{U}}\hat{\mathbf{B}})^T \hat{\mathbf{R}}^{-1} \hat{\mathbf{D}}\hat{\mathbf{U}}\hat{\mathbf{B}} \right)^{-1} \begin{bmatrix} \mathbf{1}_{p \times 1} \\ \mathbf{0}_{q \times 1} \\ \mathbf{0}_{m \times 1} \end{bmatrix} \quad (27)$$

which yields the following DS-BA-TCIMF

$$\delta^{\text{DS-BA-TCIMF}}(\mathbf{r}) = \left((\hat{\mathbf{w}})^* \right)^T \hat{\mathbf{r}} \quad (28)$$

An algorithm to implement DS-BA-TCIMF depicted in Fig. 2(a) is summarized below.

DS-BA-TCIMF	
1.	Initial condition: given value of m .
2.	1 st stage process:
	Sphere \mathbf{X} to obtained sphered data $\hat{\mathbf{X}} = \mathbf{X}_{DS}$.
3.	2 nd stage process:
a.	Implement GoDec on $\hat{\mathbf{X}}$ to produce the
	$\hat{\mathbf{X}} = \hat{\mathbf{L}} + \hat{\mathbf{S}} + \hat{\mathbf{N}} \quad (29)$
b.	Apply singular value decomposition (SVD) to $\hat{\mathbf{L}}$ and find m BKG signatures $\{\hat{\mathbf{b}}_1, \hat{\mathbf{b}}_2, \dots, \hat{\mathbf{b}}_m\}$ from $\hat{\mathbf{L}}$ to form $\hat{\mathbf{B}} = [\hat{\mathbf{b}}_1 \hat{\mathbf{b}}_2 \dots \hat{\mathbf{b}}_m]$
c.	Form $\hat{\mathbf{D}}\hat{\mathbf{U}}\hat{\mathbf{B}} = [\hat{\mathbf{d}}_1 \hat{\mathbf{d}}_2 \dots \hat{\mathbf{d}}_p, \hat{\mathbf{u}}_1 \hat{\mathbf{u}}_2 \dots \hat{\mathbf{u}}_q, \hat{\mathbf{b}}_1 \hat{\mathbf{b}}_2 \dots \hat{\mathbf{b}}_m]$.
d.	Replace \mathbf{R} in (15) with $\mathbf{R}_{BA} = \hat{\mathbf{R}}$ to perform TCIMF.

It should be noted that the OSP-target detection developed in [14] turns out to be a special case of DS-BA-TCIMF.

2) LRA-SMD-BA-TCIMF

The LRA-SMD model developed in [16] also offers a feasible solution to resolving TBS arising in TCIMF. It decomposes a data space into the low rank space \mathbf{L} , sparse space \mathbf{S} and noise space, \mathbf{N} as (14) where \mathbf{L} and \mathbf{S} can be considered as the

background and target spaces, respectively. Using the OSP specified by (2) can remove BKG, whereas finding an appropriate value of k via sparsity cardinality (SC) introduced in GoDec [16] can enhance target detectability. By including the LSaSMD model in TCIMF we can derived BA-TCIMF as follows.

Recently, LRSMD was developed to represent a data space \mathbf{X} as a three-component subspace decomposition, $\mathbf{X} = \mathbf{L} + \mathbf{S} + \mathbf{N}$ with the low rank space \mathbf{L} and sparse space \mathbf{S} corresponding to the BKG space and target space respectively and the noise space is specified by \mathbf{N} . By taking advantage of this LRSMD model, we can make use of OSP to annihilate the BKG prior to TCIMF via $P_L^\perp \mathbf{X}$ in (15).

By means of the low rank space \mathbf{L} generated by LRSMD model we can find additional unwanted BKG signals from \mathbf{L} for further improvement on BKG suppression. Using the OSP-GoDec approach proposed in [30] we can find a set of m BKG signals, $\{\mathbf{b}_1, \mathbf{b}_2, \dots, \mathbf{b}_m\}$ to form a BKG matrix $\mathbf{B} = [\mathbf{b}_1 \mathbf{b}_2 \dots \mathbf{b}_m]$ so the undesired signature matrix \mathbf{U} in (2) can be further expanded to denoted $\mathbf{DUB} = [\mathbf{d}_1 \mathbf{d}_2 \dots \mathbf{d}_p, \mathbf{u}_1 \mathbf{u}_2 \dots \mathbf{u}_q, \mathbf{b}_1 \mathbf{b}_2 \dots \mathbf{b}_m]$. As a result, (2) can be extended and expanded to

$$(\mathbf{DUB})_L^\perp = P_L^\perp (\mathbf{DUB}) \quad (30)$$

$$\text{Now, if we let } \mathbf{c} = \begin{bmatrix} \mathbf{1}_{p \times 1} \\ \mathbf{0}_{q \times 1} \\ \mathbf{0}_{m \times 1} \end{bmatrix} \text{ constrain these three target}$$

matrices by

$$((\mathbf{DUB})_L^\perp)^T \mathbf{w} = \begin{bmatrix} \mathbf{1}_{p \times 1} \\ \mathbf{0}_{q \times 1} \\ \mathbf{0}_{m \times 1} \end{bmatrix} = \left(\underbrace{1, \dots, 1}_p, \underbrace{0, \dots, 0}_q, \underbrace{0, \dots, 0}_m \right)^T \quad (31)$$

where $\mathbf{DUB} = [\mathbf{d}_1 \mathbf{d}_2 \dots \mathbf{d}_p \mathbf{u}_1 \mathbf{u}_2 \dots \mathbf{u}_q \mathbf{b}_1 \mathbf{b}_2 \dots \mathbf{b}_m]$ and $\mathbf{1}_{p \times 1}$ is a $p \times 1$ vector with ones in all components, $\mathbf{0}_{q \times 1}$ is a $q \times 1$ vector with zero in its components, and $\mathbf{0}_{m \times 1}$ is a $m \times 1$ vector with zero in its components, where the 1 represents the desired targets and 0 represents the undesired targets. Using (31) as a constraint vector, (2) can be customized-designed as following constrained optimization problem:

$$\min_{\mathbf{w}} \{ \mathbf{w}^T \mathbf{R}_{L+S} \mathbf{w} \} \text{ subject to } ((\mathbf{DUB})_L^\perp)^T \mathbf{w} = \begin{bmatrix} \mathbf{1}_{p \times 1} \\ \mathbf{0}_{q \times 1} \\ \mathbf{0}_{m \times 1} \end{bmatrix} \quad (32)$$

where the correlation matrix \mathbf{R} in (2) is replaced with \mathbf{R}_{L+S} formed by data samples in the $\mathbf{L} + \mathbf{S}$ space. The optimal solution to (20) is the weight vector $(\mathbf{w}_L^\perp)^*$ given by

$$(\mathbf{w}_L^\perp)^* = \mathbf{R}_{L+S}^{-1} (\mathbf{DUB})_L^\perp \left(((\mathbf{DUB})_L^\perp)^T \mathbf{R}_{L+S}^{-1} (\mathbf{DUB})_L^\perp \right)^{-1} \begin{bmatrix} \mathbf{1}_{p \times 1} \\ \mathbf{0}_{q \times 1} \\ \mathbf{0}_{m \times 1} \end{bmatrix} \quad (33)$$

The FIR filter specified by $(\mathbf{w}_L^\perp)^*$ in (33) is called the BA-TCIMF given by

$$\delta^{\text{LRSMD-BA-TCIMF}}(\mathbf{r}) = (\mathbf{w}_L^\perp)^* P_L^\perp \mathbf{r} \quad (34)$$

An algorithm to implement LRSMD-BA-TCIMF described in Fig. 2(b) can be summarized below.

LRSMD-BA-TCIMF

1. Initial condition: given value of m .
2. 1st stage process:
 - a. Implement DoDec to produce $\mathbf{X} = \mathbf{L} + \mathbf{S} + \mathbf{N}$ (35)
 - b. Apply P_L^\perp in (2) to remove \mathbf{L} for BKG annihilation.
3. 2nd stage process:
 - a. Apply SVD to \mathbf{L} to find m BKG signatures $\{\mathbf{b}_1, \mathbf{b}_2, \dots, \mathbf{b}_m\}$ from \mathbf{L} to form $\mathbf{B}_L = [\mathbf{b}_1 \mathbf{b}_2 \dots \mathbf{b}_m]$.
 - b. Form $(\mathbf{DU})_{L+S} \mathbf{B}_L$ and implement (20) with \mathbf{DUB} replaced by $(\mathbf{DU})_{L+S} \mathbf{B}_L$.
 - c. Replace \mathbf{R} in (15) with $\mathbf{R}_{BA} = \mathbf{R}_{L+S}$ which is the correlation matrix formed by data samples in the joint $\mathbf{L} + \mathbf{S}$ space respectively to perform TCIMF.

3) CDA-BA-TCIMF

As an alternative to LRSMD-BA-TCIMF a CDA-based BA-TCIMF can be also derived in a similar manner. It replaces the LRSMD model in (14) with the CDA model in (16) proposed by Chen et al. [17]

$$\mathbf{X} = \mathbf{PC}_m + \mathbf{IC}_j + \mathbf{N} \quad (36)$$

with \mathbf{PC}_m and \mathbf{IC}_j corresponding to \mathbf{L} and \mathbf{S} respectively. As a result of (36), a CDA-BA-TCIMF can be readily derived with its algorithm described in the following.

CDA-BA-TCIMF

1. Initial condition: given value of m .
2. 1st stage:
 - a. Implement CDA on \mathbf{X} to produce (30).
 - b. Apply $P_{\mathbf{PC}_m}^\perp$ in (4) to remove \mathbf{PC}_m space for BKG annihilation.
3. 2nd stage:
 - a. Implement SC to retain sparse signal sources. The resulting space is referred to as CDASC space.
 - b. Find the first m eigenvectors from the CDASC space as BKG signatures $\{\mathbf{b}_1, \mathbf{b}_2, \dots, \mathbf{b}_m\}$ from \mathbf{PC}_m to form $\mathbf{B}_{\mathbf{PC}_m} = [\mathbf{b}_1 \mathbf{b}_2 \dots \mathbf{b}_m]$.
 - c. Form $\mathbf{D}_c \mathbf{U}_c \mathbf{B}_{\mathbf{PC}_m}$ and implement (20) with \mathbf{DUB} replaced by $(\mathbf{D}_c \mathbf{U}_c)_{\mathbf{PC}_m} \mathbf{B}_{\mathbf{PC}_m}$.
 - d. Replace \mathbf{R} in (15) with $\mathbf{R}_{BA} = \mathbf{R}_{\mathbf{PC}_m + \mathbf{IC}_j}$ which is the correlation matrix formed by data sample the joint $\mathbf{PC}_m + \mathbf{IC}_j$ respectively to perform TCIMF.

Fig. 2(c) depicts the diagram of CDA-BA-TCIMF where BKG is annihilated by CDA.

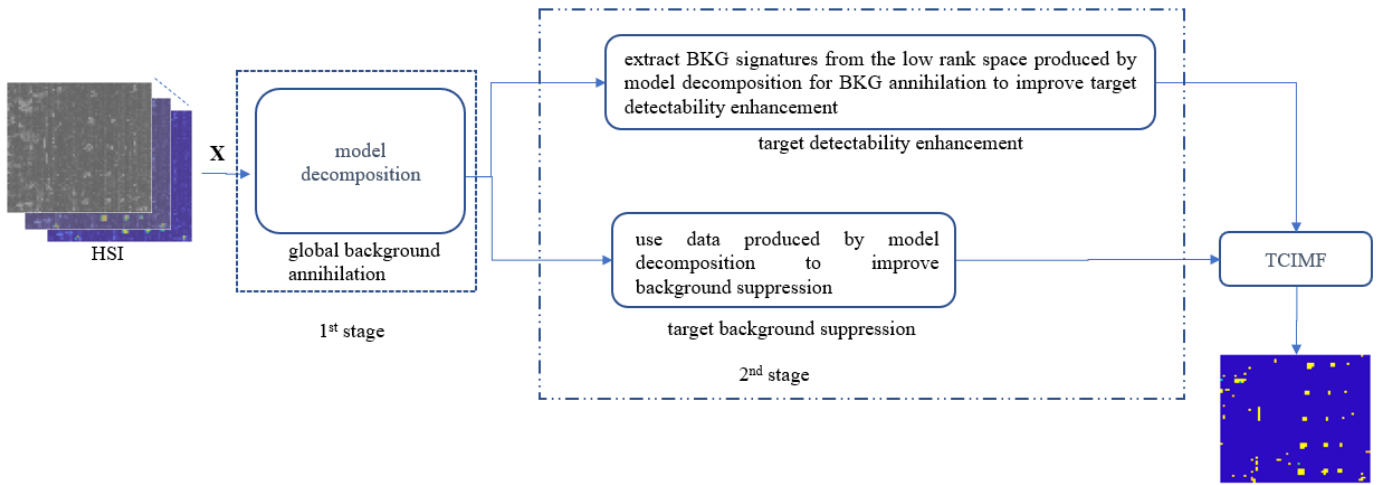
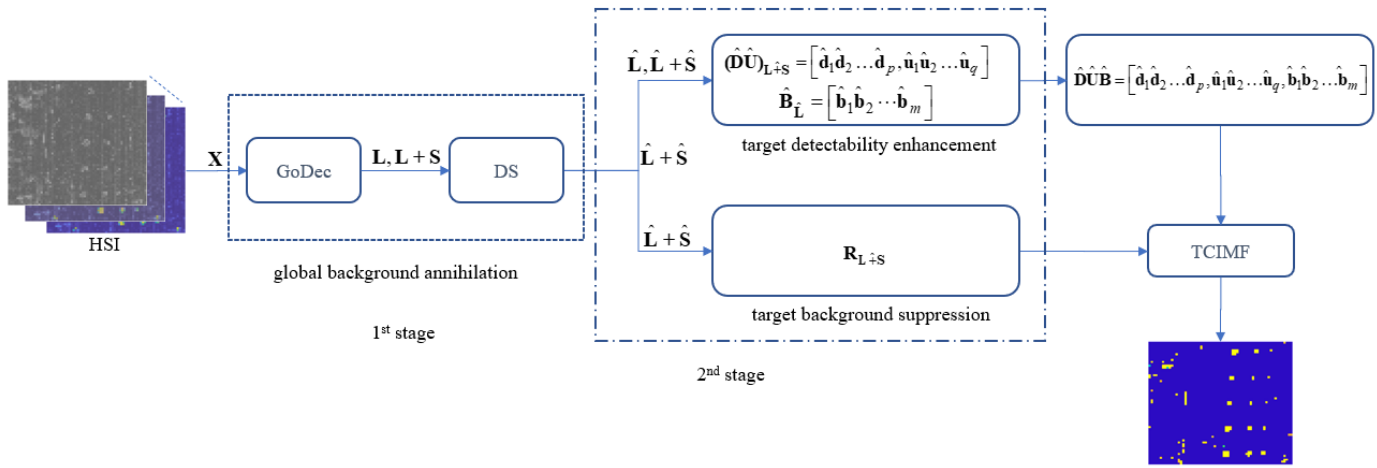
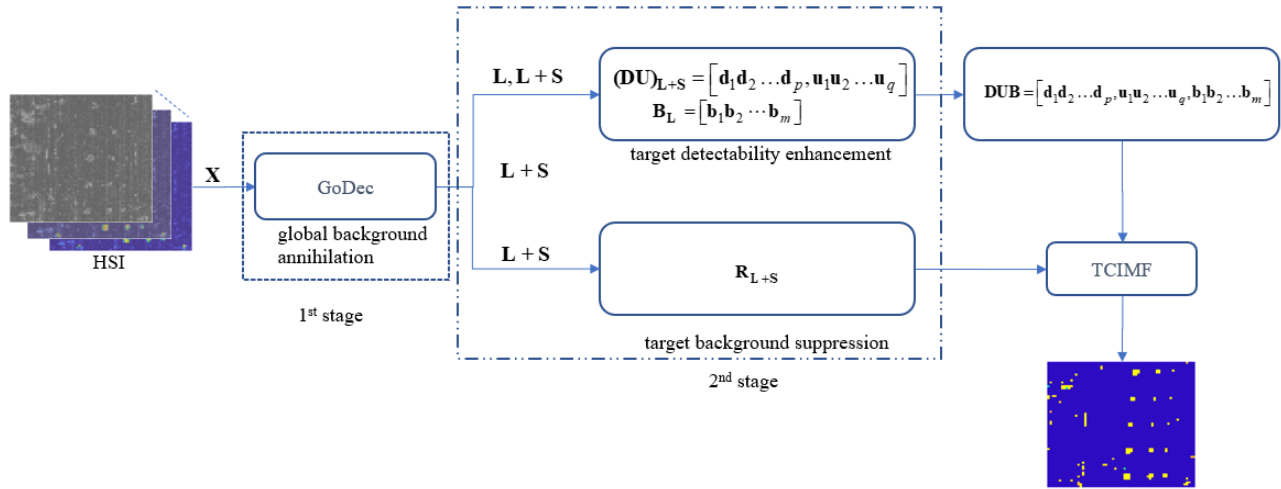


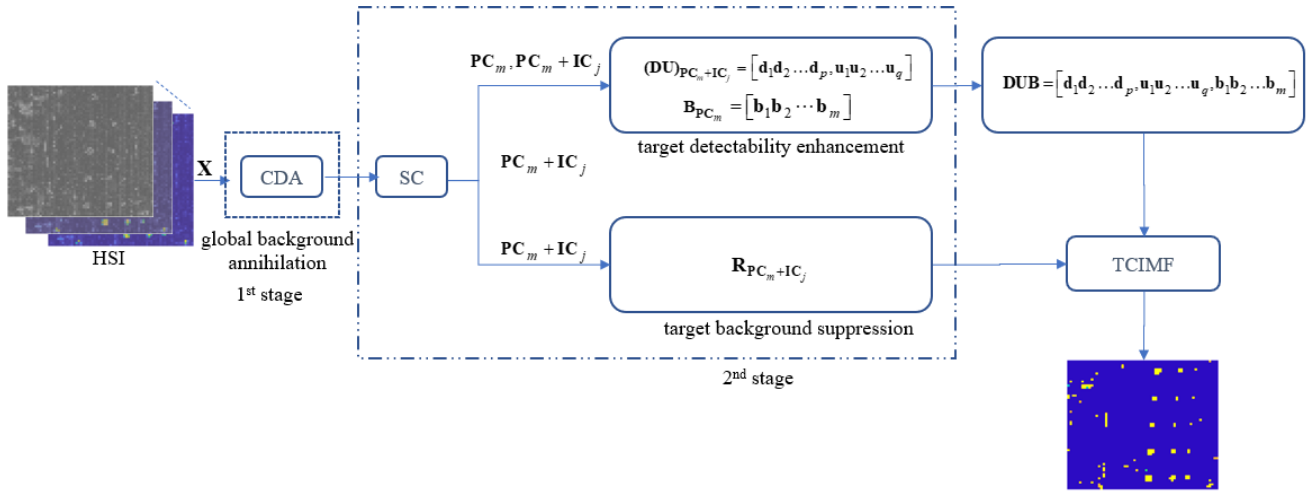
Fig. 1. Two stages implemented in BA-TCIMF



(a) Diagram of DS-BA-TCIMF implemented in two stages



(b) Diagram of LRaSMD-BA-TCIMF implemented in two stages



(c) Diagram of CDA-BA-TCIMF implemented in two stages

Fig. 2. Diagrams of three versions of BA-TCIMF

IV. IMAGE DATA AND DETECTION MEASURES

A. HYDICE Data Scene

Fig. 3 shows that the image scene to be studied was captured in August 1995 by the aerial hyperspectral digital imagery collection experiment (HYDICE) sensor from a flight altitude of 10000 ft. This scene has been investigated in depth by many reports such as [1-4]. It has size of 64×64 pixel vectors where low signal/high noise bands: bands 1-3 and bands 202-210; and water vapor absorption bands: bands 101-112 and bands 137-153 were removed to yield 169 spectral bands. The spatial resolution is 1.56m and spectral resolution is 10nm. The scene is consisting of 15 square panels with three different sizes, $3\text{ m} \times 3\text{ m}$, $2\text{ m} \times 2\text{ m}$ and $1\text{ m} \times 1\text{ m}$ respectively shown in Fig. 3(a). Since the ground sampling distance is approximately 1.56 m, the panels in the 1st column except the 1st row have two-panel pixels which are highlighted by red, p_{211} , p_{221} in row 2, p_{311} , p_{312} in row 3, p_{411} , p_{412} in row 4, p_{511} , p_{521} in row 5 as shown in Fig. 3(b) in the ground truth. All the remaining 11 panels in Fig. 3(b) only contain one single panel pixel for each panel also highlighted by red, p_{11} , p_{12} , p_{13} in row 1, p_{22} , p_{23} in row 2, p_{32} , p_{33} in row 3, p_{42} , p_{43} in row 4, p_{52} , p_{53} in row 5. Adding them up, the scene has a total of 19-panel pixels. Their precise spatial locations are shown in Fig. 3(b) with the pixels in yellow (Y pixels) indicating panel pixels mixed with the BKG. The five-panel spectral signatures are plotted in Fig. 3(c), p_1 , p_2 , p_3 , p_4 , and p_5 , which were obtained from Fig. 3(b), where p_i is the i^{th} panel signature, was calculated by averaging the red panel pixels in row i .

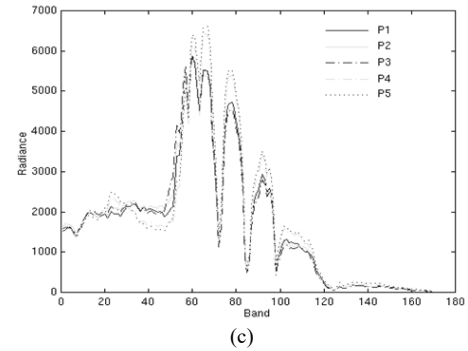


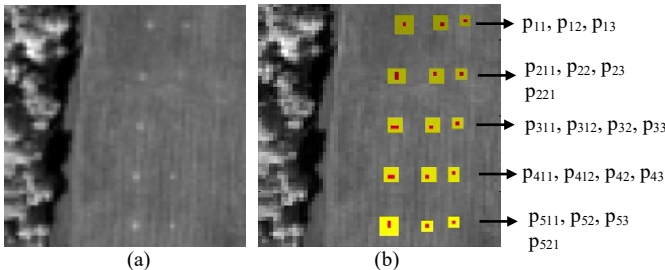
Fig. 3. (a) A HYDICE panel scene which contains 15 panels; (b) Ground truth map of spatial locations of 19 R panel pixels; (c) Spectra of p_1 , p_2 , p_3 , p_4 and p_5

This particular scene was used for subpixel target detection of panel pixels in the 3rd column and mixed target detection of panel pixels highlighted by yellow in the 1st and 2nd columns. Detailed descriptions of this data scene and discussions on experiments can be found in [1, sections 9.3 and 9.4] and [2-3].

One major key issue in implementing GoDec is determinization of the values of r and k , which are the order of low rank subspace L and the sparsity of a sparse subspace S respectively. The OSP-GoDec proposed in [1, 19-23] used VD and minimax singular value decomposition (MXSVD) that was derived from the maximum orthogonal complement algorithm (MOCA) developed in [23] to resolve this issue. Instead of directly estimating r and k , it first used VD to estimate a parameter p which is assumed to be the number of spectral signatures. The value of p can be used to determine the sum of the order of L , denoted by m and the rank of S , denoted by j as $p = m + j$. As a result, r and k used in GoDec can be obtained by letting $r = m = p - j$ and $k = j \times N$. In the following experiments, the same idea of using VD/MXSVD were also used to estimate m as r and $k = j \times N$ for GoDec.

B. AVIRIS San Diego Airport Scene

Fig. 4(a) shows a second data scene to be studied is an AVIRIS airport scene from San Diego, CA, USA. The size of the airport is 400×400 pixels, and its spatial resolution is 3.5m with 224 spectral bands which is the third dimensionality ranging from 370 to 2510 nm. Some bands corresponding to



the water absorption regions, the low signal-to-noise ratio, and collapse bands (1–6, 33–35, 97, 107–113, 153–166, and 221–224) have been removed and finally results in 189 bands. A red square was marked at the upper left corner of the scene was chosen as the test image with its ground-truth image shown in Fig. 4(b) and Fig. 4(c), respectively. The restricted area has a size of 100×100 pixels. the BKG of the scene is mainly made up of a roof, shadow, and grass. The targets that we are interested in are three airplanes with the same materials in the scene, which comprised 85 pixels and account for 0.33% of the test image as shown in Fig. 4(b). The location of these planes can be obtained from the ground truth in Fig. 4(c) and then be used as the desired signature \mathbf{d} .



(a) pseud-color image of the whole scene



(b) pseud-color image of the selected area (c) the ground truth map



To estimate VD, HFC and its noise-whitened HFC (NWHFC) [1,19,38] were used to estimate p . This was followed by MXSVD to estimate j . Table I tabulates the value of p and j estimated by $P_F \leq 10^{-3}$ and MX-SVD so that $m = p - j$ and $k = j \times N$ and parameter setting for KTCIMF. In the following experiments, γ was set to 2 [16] and $\varepsilon = 10^{-3}$. It should be noted that the parameter q used in GoDec to address the singular value decay problem is now replaced by γ because the q is used by TCIMF in (25) as the number of undesired target signatures.

TABLE I
PARAMETERS OF p AND j ESTIMATED BY NWHFC USING MX-SVD FOR HYDICE AND SAN DIEGO AIRPORT DATA SETS AND PARAMETER SETTINGS FOR KTCIMF

estimation of p and j by NWHFC using MX-SVD			
Data	VD	p	j by MX-SVD
HYDICE 15-panel scene	NWHFC $P_F \leq 10^{-3}$	13	6
San Diego airport scene	HFC, $P_F \leq 10^{-3}$	10	2
parameter setting for KTCIMF			
Data	kernel	standard deviation	
HYDICE 15-panel scene	Gaussian	4.92×10^{-11}	
San Diego airport scene	Gaussian	5.88×10^{-12}	

It should be noted that in the following experiments, the four parameters, r , k , ε , γ used in the original GoDec were implemented by letting r to $m = p - j$ and γ to 2. The experiments for different settings of j and p have been studied in great detail in references [14-15,17,30]. The values used in this paper were selected from the best cases reported in these references.

In addition, the computer environment used for experiments is documented in Table II.

TABLE II
COMPUTER ENVIRONMENT

computer environment parameter	configuration
OS Name:	Microsoft Windows 10 Home
OS Version:	10.0.19043 N/A Build 19043
OS Manufacturer:	Microsoft Corporation
System Type:	x64-based PC
Processor(s):	Intel(R) Core(TM) i7-8750H CPU @ 2.20GHz 2.21 GHz
Total Physical Memory:	32,624 MB
Graphics Card:	GeForce GTX 1060 Graphics Cards

C. Target Detection Measures

1) Targets Detection Measure

In [26], it is noted that $AUC_{(D,F)}$ cannot fully evaluate a detector, and it can be only used to evaluate the effectiveness of a detector. By taking the factor $AUC_{(D,\tau)}$ into $AUC_{(D,F)}$ account, then a new target detectability measure that derive from both 2D ROC curve of (P_D, P_F) and 2D ROC curve of (P_D, τ) , denoted by AUC_{TD} as follows is established.

$$0 \leq AUC_{TD} = AUC_{(D,F)} + AUC_{(D,\tau)} \leq 2. \quad (37)$$

2) Joint Target Detection BKG Suppression Measure

In the Neyman Pearson detection theory, it maximizes P_D by fixing P_F . Therefore, P_D and P_F are two critical factors to evaluate the performance of a detector. By just using P_D to solely evaluate the detection performance is not enough and reasonable since BKG has a tremendous impact on target detection and worth paying extra consideration in detecting targets where the targets and BKG are mixed and be embedded at the subpixel level. Thus, to measure the performance of BKG suppression in hyperspectral target detection, P_F is introduced. But current measurements used P_D and P_F separately, to measure a detector more comprehensively, using a joint target detection and BKG suppression (TDBS) measurement is more suitable than using P_D and P_F solely and separately. Taking P_F into different considerations, two detection measures related to P_F can be derived as follows.

One of them is called BKG suppression measure defined by

$$-1 \leq AUC_{BS} = AUC_{(D,F)} - AUC_{(F,\tau)} \leq 1. \quad (38)$$

It measures the effectiveness of detectors by taking P_F into consideration carefully.

The other is target detection and BKG suppression (TDBS) defined by

$$-1 \leq AUC_{TDBS} = AUC_{(D,\tau)} - AUC_{(F,\tau)} \leq 1 \quad (39)$$

It measures the target detection ability by taking P_F into consideration carefully.

3) Signal to Noise Probability Ratio

The idea of signal-to-noise ratio (SNR), which is extensively used in communication, can also be utilized to create a detection measure termed signal-to-noise probability ratio, similar to AUC_{TDBS} (SNPR), denoted by AUC_{SNPR} , as

$$0 \leq AUC_{SNPR} = \frac{AUC_{(D,\tau)}}{AUC_{(F,\tau)}} \quad (40)$$

where $AUC_{(D,\tau)}$ can be viewed as signals, and $AUC_{(F,\tau)}$ can be viewed as noise.

There is a significant difference between SNR and SNPR. SNR is widely used in communications and signal processing which calculates the ratio of signal energy to noise energy. SNPR calculates the ratio of $AUC_{(D,\tau)}$ to $AUC_{(F,\tau)}$, both of which are probabilities where $AUC_{(D,\tau)}$ and $AUC_{(F,\tau)}$ correspond to target detection probability solely determined by the threshold τ and false alarm probability also solely determined by the threshold τ respectively.

4) Overall Detection Measure

As you may be noticed that TD in (37), BS in (38), TDBS in (39), and SNPR in (40) all only considered the two 2D ROC curves. This section derives a new detection measure by taking into account AUC values of its corresponding three 2D ROC curves, 2D ROC curves of (P_D, P_F) , 2D ROC curves of $(P_{D,\tau})$, 2D ROC curves of $(P_{F,\tau})$, named overall detection probability (ODP), denoted by AUC_{ODP} , as

$$-1 \leq AUC_{ODP} = AUC_{(D,F)} + AUC_{(D,\tau)} - AUC_{(F,\tau)} \leq 2 \quad (41)$$

This detection measure tends to measure how effectiveness and detection performance of a detector by considering the impact of BKG suppression. The reason is that higher values of $AUC_{(D,F)}$ and $AUC_{(D,\tau)}$ mean higher detection performance. Conversely, a lower value of $AUC_{(F,\tau)}$ indicates a better BKG suppression and thus, a better detection performance. As a result, (41) combines the AUC values obtained by the three 2D ROC curves to provide a single quantitative measurement of overall detection performance.

Because $AUC_{(F,\tau)}$ indicates false alarm probability, $1-AUC_{(F,\tau)}$ is actually no-signal predictive probability in [19] or no-signal detectability. As a result, we may develop a new detection measure by replacing $AUC_{(F,\tau)}$ with $1-AUC_{(F,\tau)}$, denoted by AUC_{ODP} , as

$$0 \leq AUC_{ODP} = AUC_{(D,F)} + AUC_{(D,\tau)} + (1-AUC_{(F,\tau)}) \leq 3 \quad (42)$$

This is the same as (41) and can be used to assess a detector's overall performance in terms of effectiveness, target detectability, and no-signal detectability.

If we believe that signal sources and BKG sources are two distinct groups of sources, used C_S to represent the signal class, and used C_{BKG} to indicate the BKG class, along with their class sample ratios determined by $p_S = \frac{n_S}{N}$ and

$$p_{BKG} = \frac{n_{BKG}}{N} \text{ respectively, where } n_S, n_{BKG}, \text{ and } N \text{ represent}$$

the number of data samples in signal class, C_S and the BKG class, C_{BKG} and the total number of data samples. Then formula (42) can be modified by letting $AUC_{(D,F)}$ be zero to

remove it, and it was reduced to overall accuracy (OA) for a two-class (signal,BKG) classification problem defined by

$$0 \leq OA = p_S AUC_{(D,\tau)} + p_{BKG} (1-AUC_{(F,\tau)}) \leq 1. \quad (43)$$

As a result, formula (43) can be considered as a special case of (36).

To facilitate the use of 2D/3D ROC analysis Matlab-based software codes developed for calculating AUC and plotting ROC are made available at the website of the Remote Sensing Signal and Image Processing Laboratory (RSSIPL), University of Maryland, Baltimore County (UMBC)².

V. EXPERIMENTS AND DISCUSSIONS

This section performs HYDICE and San Diego experiments to evaluate detection performance of various targeted detectors developed most recently in the literature, TCIMF, CEM, OSPTD implemented by $(\hat{L}, \hat{L} + \hat{S})$ -OSP [14], DS-BA-TCIMF, LRA-SMD-BA-TCIMF and hierarchical HCEM [21] and ensemble-based (ECEM) [22]. For the HYDICE experiments, the target \mathbf{d} is specified by one of 5-panel signatures in Fig. 3(c), and the remaining 4 panel signatures will be treated as undesired target signatures, \mathbf{U} . For San Diego experiments, since it only has one target specified by the three airplanes in the scene, there is no undesired target signature matrix \mathbf{U} . In this case, TCIMF was implemented with $\mathbf{U} = \emptyset$ as an empty set. For OSPTD, DS-BA-TCIMF, LRA-SMD-BA-TCIMF the sphered low rank and low-rank matrices were used as undesired target signature matrices, respectively where the low-rank matrix and sparsity matrix were generated by GoDec described in Section II.C.

A. HYDICE Data Experiments

Figs. 5(a-n) show the detection maps produced by OSP, CEM, SDIA, TCIMF, KTCIMF, OSPTD, DS-BA-TCIMF/KTCIMF, LRA-SMD-BA-TCIMF/KTCIMF, HCEM and ECEM. By visual inspection of Fig. 5 the best results were those produced by BA-KTCIMF where not only the spatial coordinates of 19 R panel pixels were precisely located but also BKG was completely suppressed as shown in Figs. 5(b), 5(d), 5(f), 5(j) by BA-KTCIMF and Figs. 5(m) by HCEM, Fig. 5(n) by ECEM. This was followed by the next best results produced by BA-TICMF without using kernels shown in Figs. 5(a), 5(c), 5(e). Due to the use of the joint matrix of $\mathbf{L} + \mathbf{S}$, the 19 R panel pixels were precisely detected. The five subpixel panels in the 3rd column which are subpixel also were identified clearly. What are the most interestingly is the spatial locations of p_{211} and p_{221} which are vertically lined up in the 2nd row, and the spatial location of p_{311} and p_{312} which are horizontally lined up in 3rd row, and the spatial location of p_{411} and p_{412} which are horizontally lined-up in the 4th row, and the spatial location of p_{511} and p_{521} which are vertically lined-up in 5th row shown in Fig. 3(b) by ground truth were correctly detected without any blur. The worst result was produced by OSP in Fig. 5(g) followed by the second worst result by SDIA in Fig. 5(k). This mainly due to the fact that panel detection was largely caused by the complicated BKG and the similarity of panels of each row. But this dilemma was

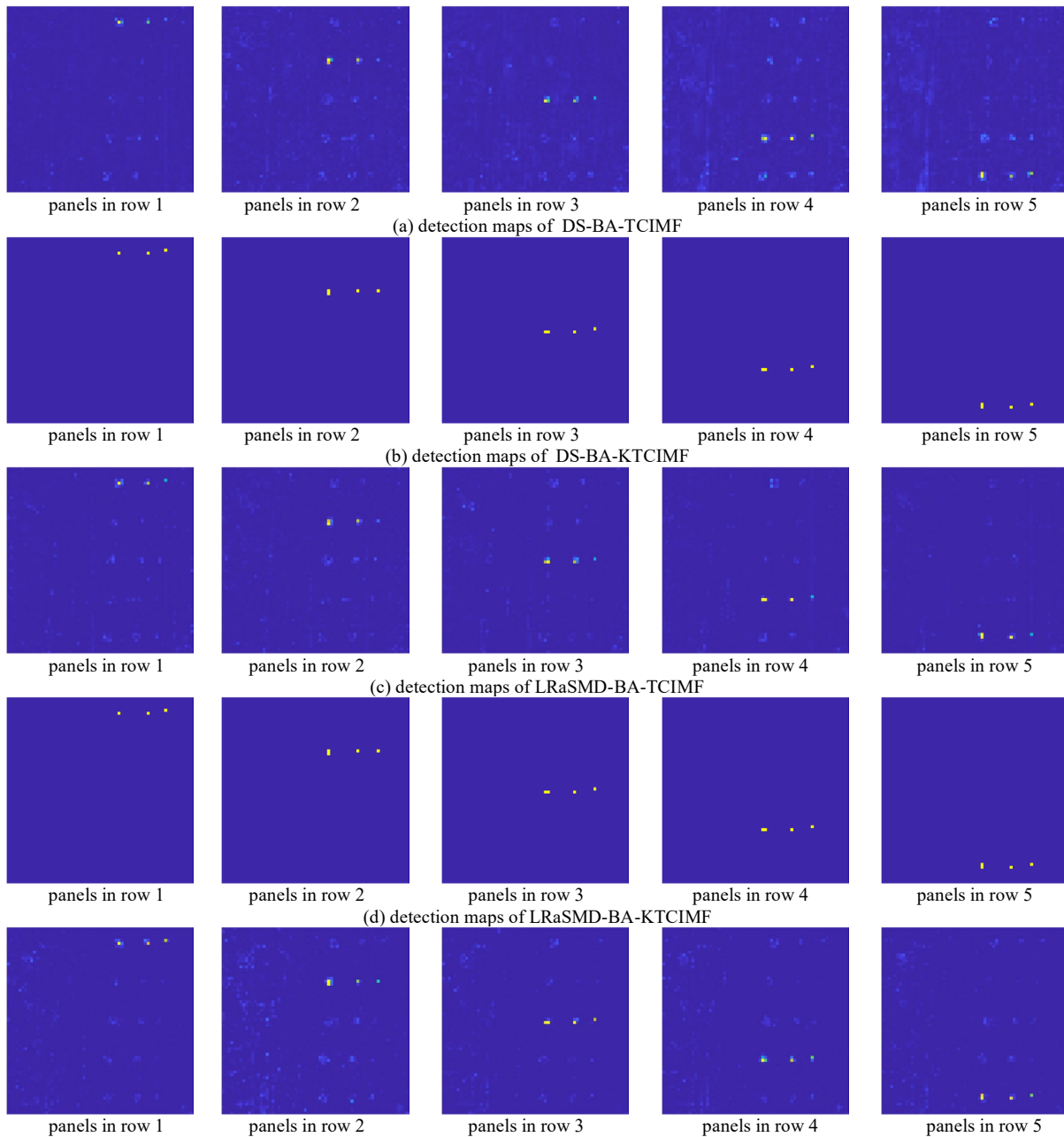
² <https://wiki.umbc.edu/display/rssipl/10.+Download>

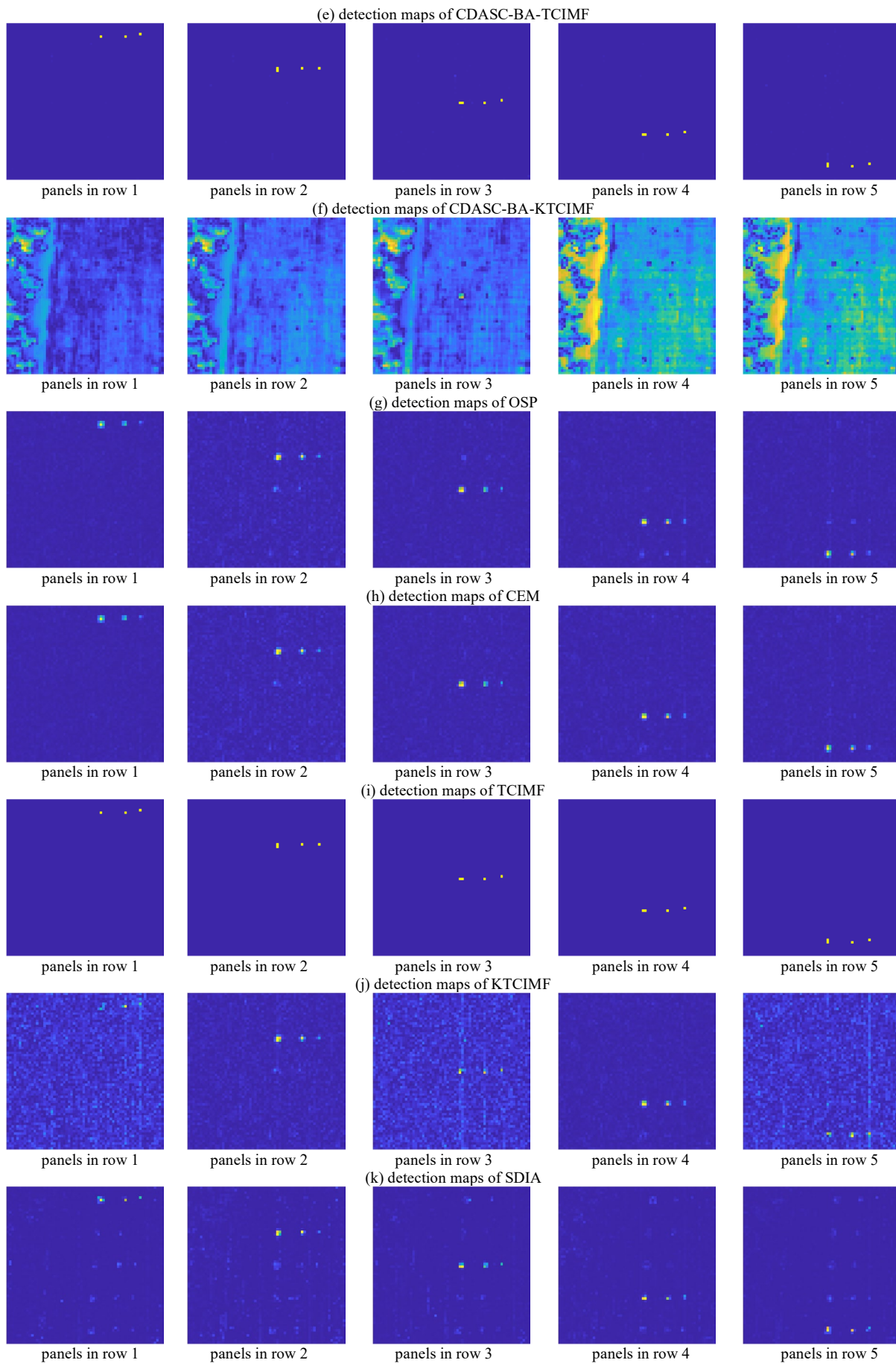
effectively resolved by TCIMF in Fig. 5(i) and further improved by including data sphering in Figs. 5(a), 5(c) and 5(e). In particular, the detection results by OSP in Fig. 5(g) was amazingly improved by OSPTD in Fig. 5(l) by simply using data sphering to annihilate BKG prior to panel detection. The results in Figs. 5(a), 5(c), 5(e) and 5(l) indicated that BKG can be largely characterized by first and second-order statistics. Besides, the results in Figs. 5(a), 5(c), 5(e) also showed that BA-TCIMF could be significantly improved by using the low-rank matrix \mathbf{L} as a BKG signature matrix for global BKG annihilation or using P_L^\perp to annihilate global BKG. Interestingly, both BA-TCIMF and $(\hat{\mathbf{L}}, \hat{\mathbf{L}} + \hat{\mathbf{S}})$ -OSP share the same concept that BKG must be annihilated prior to target detection.

To further conduct quantitative studies and analysis, 3D ROC curves of the detection results in Fig. 5 along with their

corresponding 2D ROC curves are plotted in Fig. 6 from which the eight detection measures derived in Section IV.C were calculated in Table III for performance evaluation with best in bold, second-best in bold red and third-best in bold blue. As also shown in the last column of Table III are the computing times.

As shown in Table III, all the KTCIMF-based detectors performed extremely well in all detection measures across board and achieved perfect panel detection at the expense of exceedingly high computational complexity. Their corresponding counterparts, BA-TCIMF produced the second-best results with only inappreciable performance degradation. So, if we factor in the issue of computing time, BA-TCIMF is generally preferred to BA-KTCIMF. Also, Table III showed that the best and second-best results were very close but the third-best results were little far off from the best results.





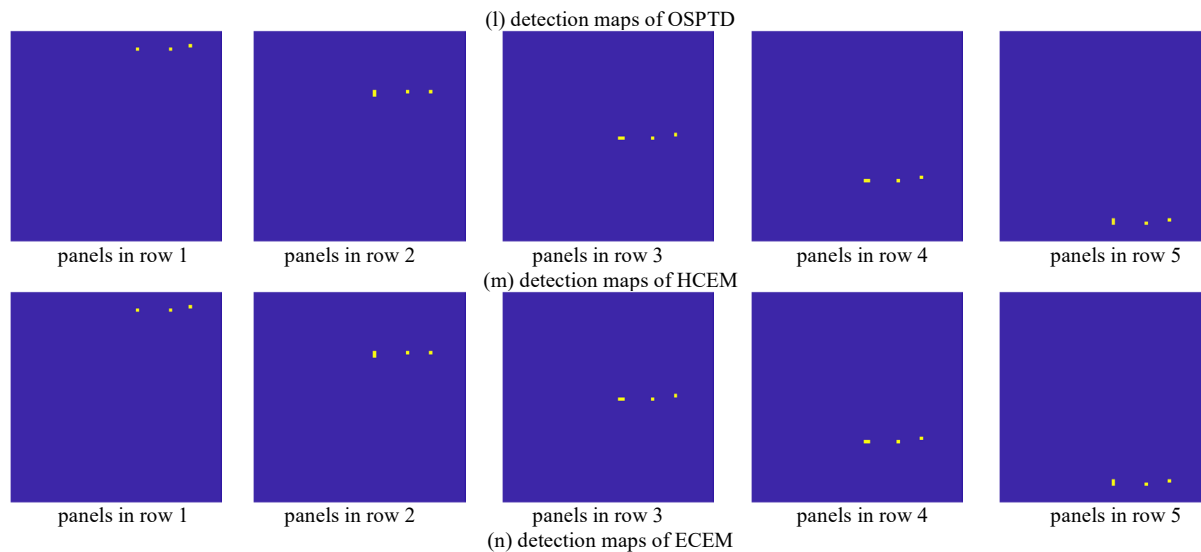
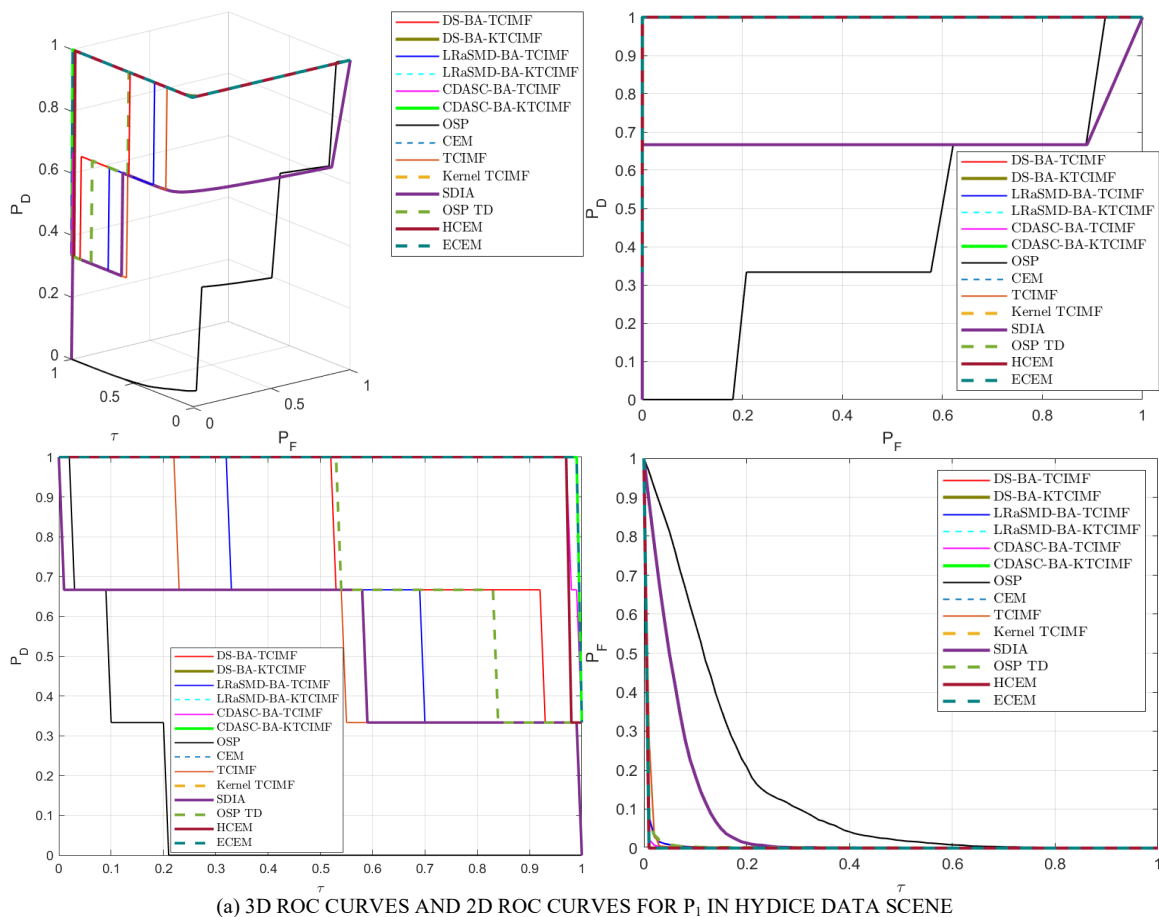
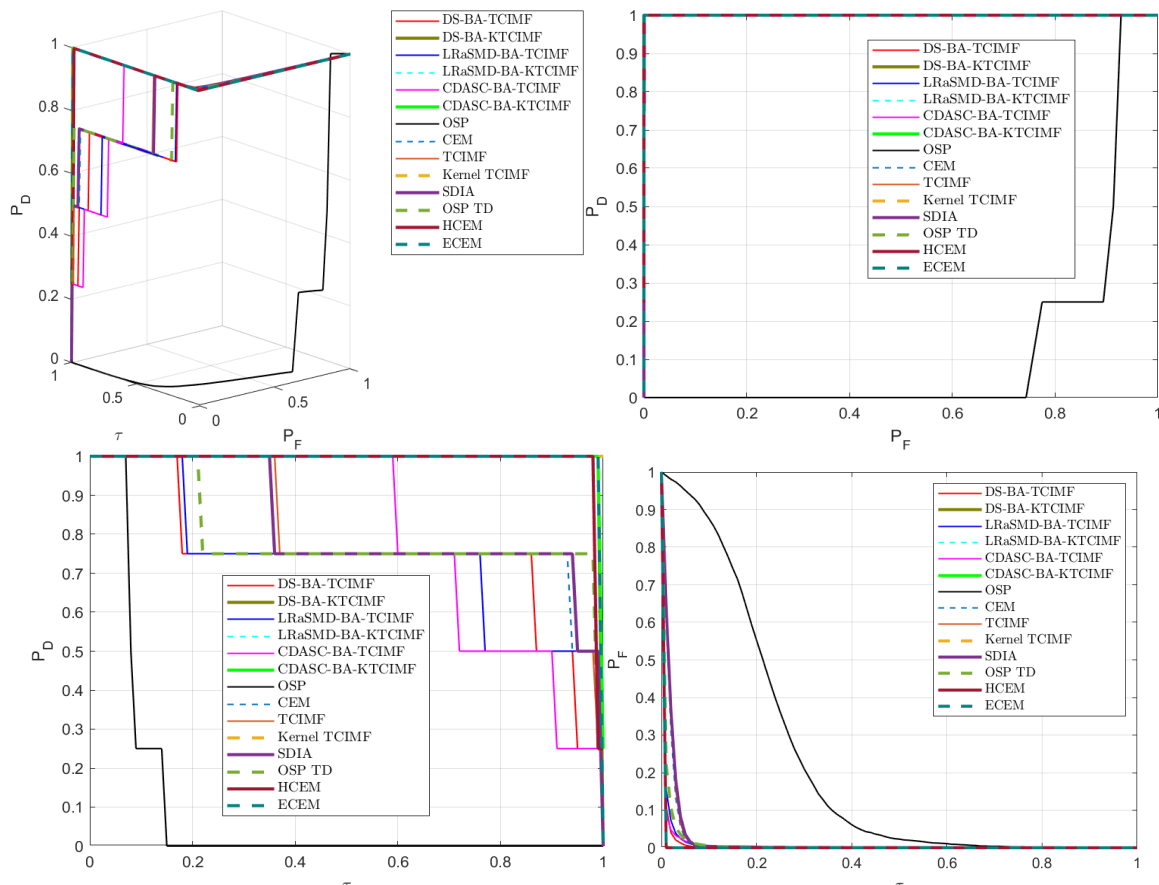
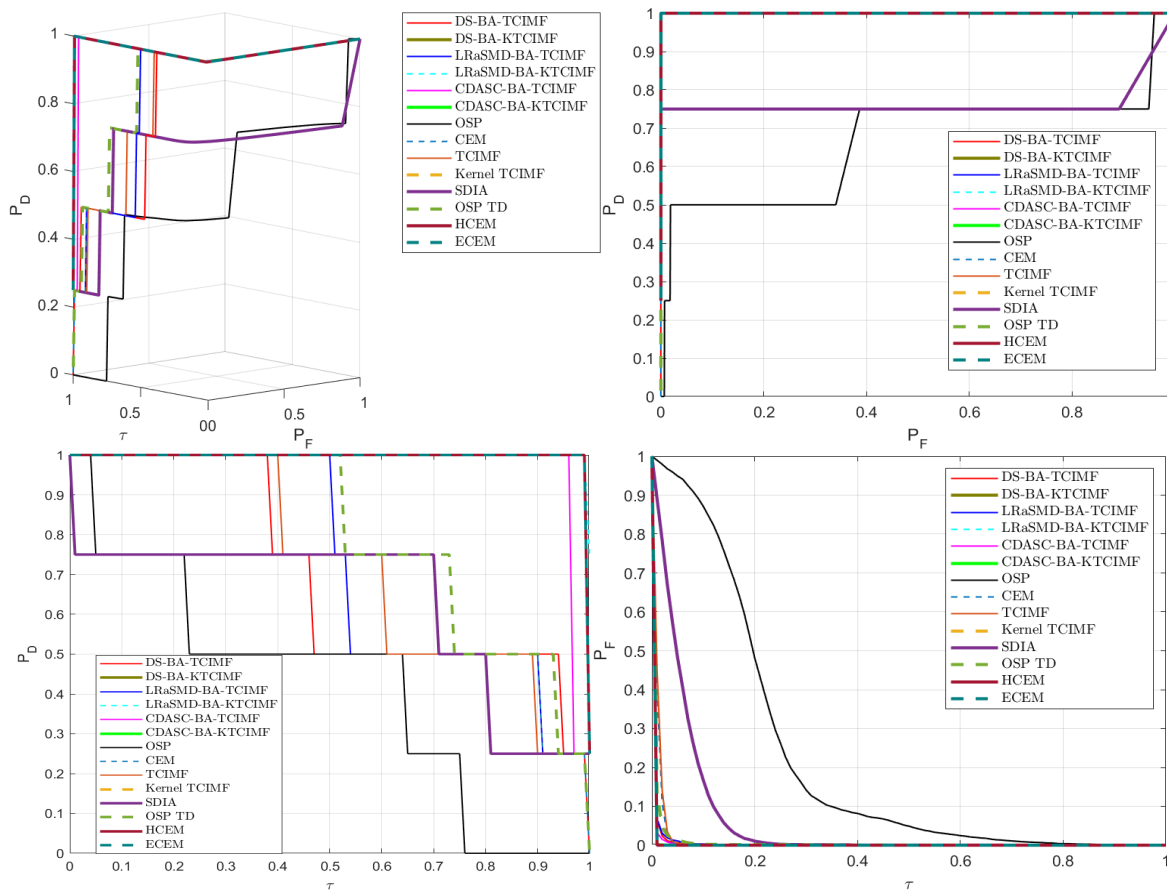


Fig. 5. target abundance detection maps of various target detectors for HYDICE data scene

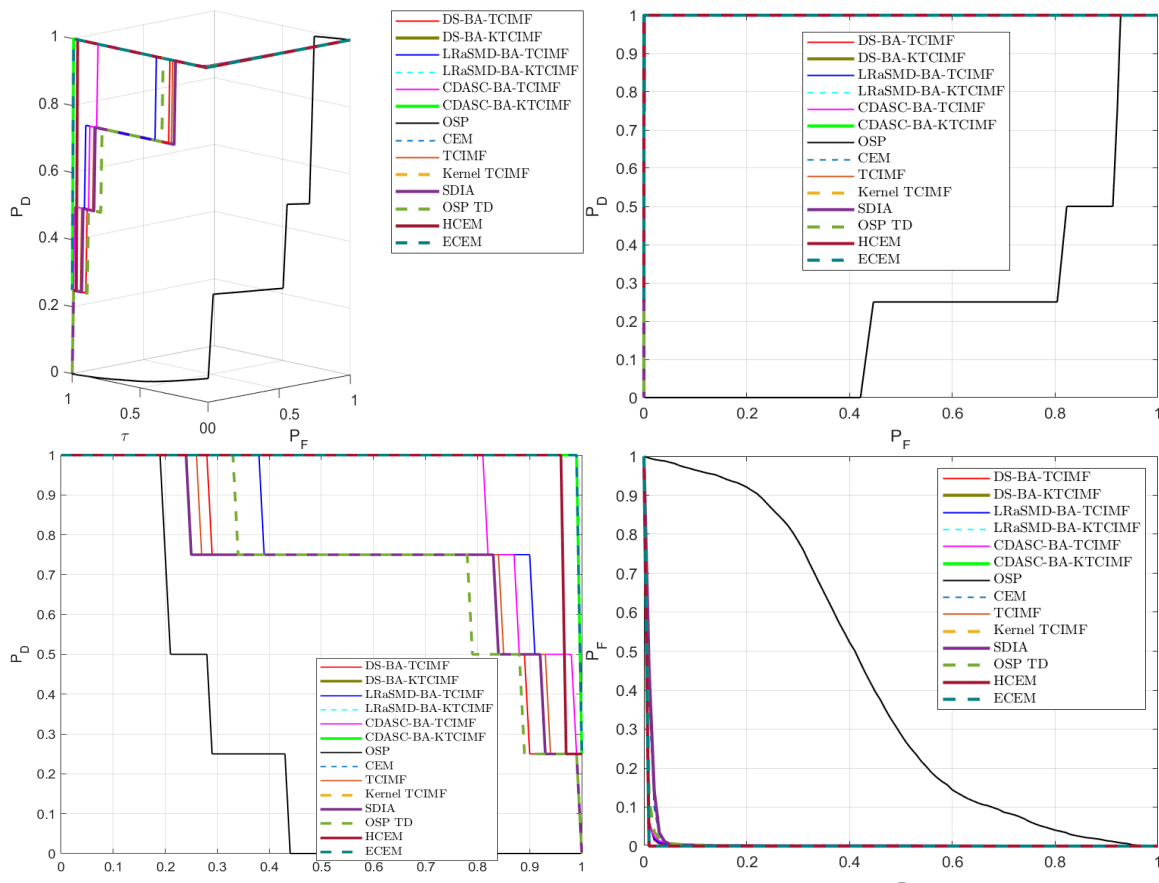




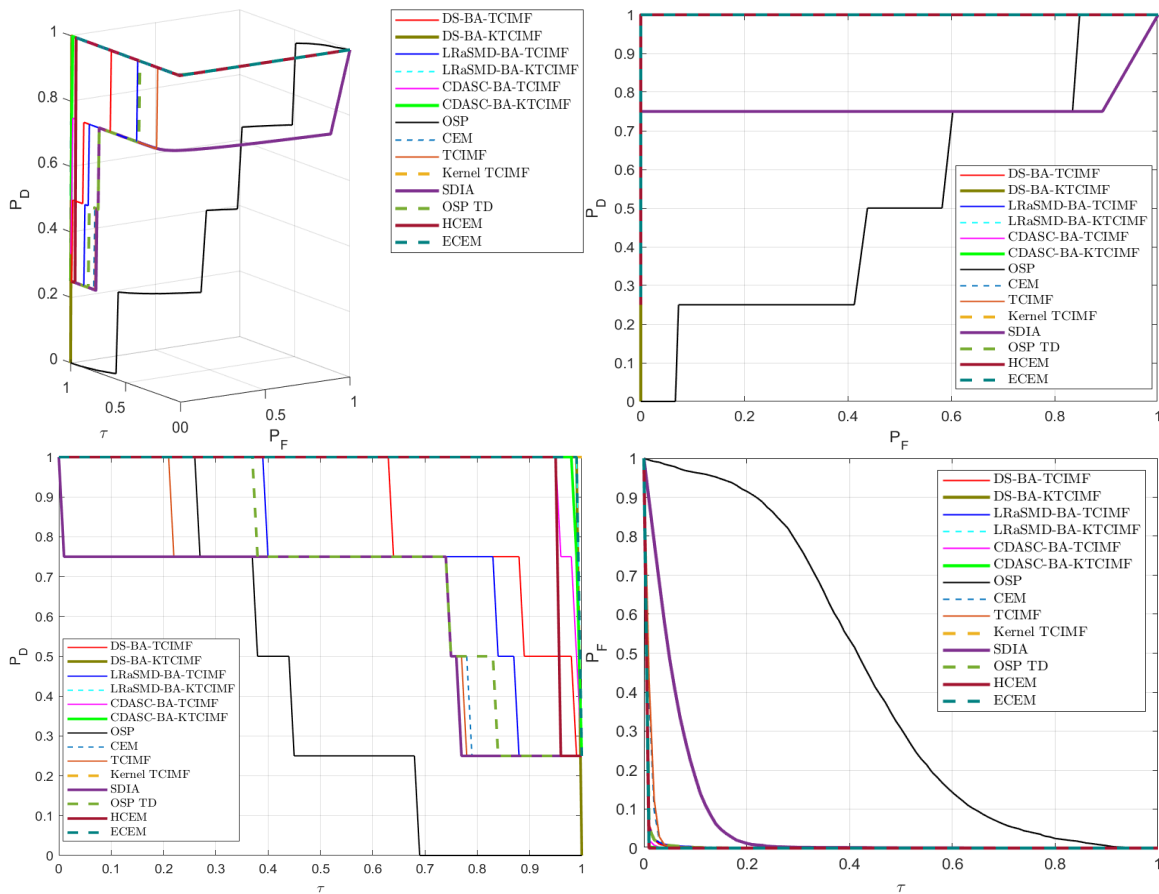
(b) 3D ROC CURVES AND 2D ROC CURVES FOR P_2 IN HYDICE DATA SCENE



(c) 3D ROC CURVES AND 2D ROC CURVES FOR P_3 IN HYDICE DATA SCENE



(d) 3D ROC CURVES AND 2D ROC CURVES FOR P_4 IN HYDICE DATA SCENE



(e) 3D ROC CURVES AND 2D ROC CURVES FOR P_5 IN HYDICE DATA SCENE

Fig. 6. ROC curves generated from the results in Fig. 5 for HYDICE data scene

TABLE III
AUC VALUES CALCULATED FROM THE THREE 2D ROC CURVES FOR FIVE ROWS DETECTION RESULTS

d	detector	AUC _(D,F)	AUC _(D,x)	AUC _(F,x)	AUC _{TD}	AUC _{BS}	AUC _{TDBS}	AUC _{SNPR}	AUC _{ODP}	Time(s)
p ₁	DS-BA-TCIMF	1.0000	0.6900	0.0085	1.6900	0.9915	0.6815	80.8639	1.6815	3.3254
	DS-BA-KTCIMF	1.0000	0.9967	0.0050	1.9967	0.9950	0.9917	199.3333	1.9917	283.5625
	LRaSMD-BA-TCIMF	1.0000	0.6267	0.0068	1.6267	0.9932	0.6199	92.4472	1.6199	2.9029
	LRaSMD-BA-KTCIMF	1.0000	0.9967	0.0050	1.9967	0.9950	0.9917	199.3333	1.9917	125.1055
	CDASC-BA-TCIMF	1.0000	0.9900	0.0053	1.9900	0.9947	0.9847	185.1528	1.9847	0.8918
	CDASC-BA-KTCIMF	1.0000	0.9967	0.0050	1.9967	0.9950	0.9917	198.8475	1.9917	105.7600
	OSP [5]	0.4333	0.1083	0.1430	0.5416	0.2903	-0.0347	0.7574	0.3986	1.3042
	CEM [7-8]	0.9993	0.5883	0.0090	1.5876	0.9903	0.5793	65.3030	1.5786	1.1518
	TCIMF [10]	0.9993	0.5883	0.0090	1.5876	0.9903	0.5793	65.4628	1.5786	0.7553
	KTCIMF [18]	1.0000	1.0000	0.0050	2.0000	0.9950	0.9950	200.0000	1.9950	45.7554
	SDIA [12]	0.6852	0.5283	0.0603	1.2135	0.6248	0.4680	8.7576	1.1532	0.7694
	OSPTD [14]	1.0000	0.6633	0.0068	1.6633	0.9932	0.6566	98.2458	1.6566	3.1729
	HCEM [21]	1.0000	0.9833	0.0050	1.9833	0.9950	0.9783	196.6667	1.9783	0.7807
	ECEM [22]	1.0000	0.9967	0.0050	1.9967	0.9950	0.9917	199.3333	1.9917	15.6134
p ₂	DS-BA-TCIMF	1.0000	0.8588	0.0108	1.8588	0.9892	0.8479	79.3946	1.8479	3.1457
	DS-BA-KTCIMF	1.0000	0.9963	0.0050	1.9963	0.9950	0.9913	199.2500	1.9913	282.2028
	LRaSMD-BA-TCIMF	1.0000	0.7438	0.0075	1.7438	0.9925	0.7362	98.9410	1.7362	2.7293
	LRaSMD-BA-KTCIMF	1.0000	0.9963	0.0050	1.9963	0.9950	0.9913	199.2500	1.9913	127.1160
	CDASC-BA-TCIMF	1.0000	0.9738	0.0057	1.9738	0.9943	0.9681	172.1203	1.9681	0.7122
	CDASC-BA-KTCIMF	1.0000	0.9963	0.0050	1.9963	0.9950	0.9912	197.9920	1.9912	125.3686
	OSP [5]	0.6643	0.4175	0.2162	1.0818	0.4480	0.2013	1.9307	0.8655	1.4318
	CEM [7-8]	0.9997	0.7275	0.0112	1.7272	0.9885	0.7163	64.8427	1.7160	1.2721
	TCIMF [10]	0.9997	0.7263	0.0120	1.7259	0.9877	0.7142	60.3537	1.7139	0.5656
	KTCIMF [18]	1.0000	1.0000	0.0050	2.0000	0.9950	0.9950	200.0000	1.9950	44.5655
	SDIA [12]	0.7636	0.6288	0.0582	1.3923	0.7053	0.5705	10.7980	1.3341	0.5977
	OSPTD [14]	1.0000	0.7550	0.0072	1.7550	0.9928	0.7478	104.9766	1.7478	3.0110
	HCEM [21]	1.0000	0.9963	0.0050	1.9963	0.9950	0.9913	199.2500	1.9913	0.5979
	ECEM [22]	1.0000	0.9963	0.0050	1.9963	0.9950	0.9913	199.2500	1.9913	15.6970
p ₃	DS-BA-TCIMF	1.0000	0.8588	0.0108	1.8588	0.9892	0.8479	79.3946	1.8479	3.1443
	DS-BA-KTCIMF	1.0000	0.9963	0.0050	1.9963	0.9950	0.9913	199.2500	1.9913	283.1608
	LRaSMD-BA-TCIMF	1.0000	0.7438	0.0075	1.7438	0.9925	0.7362	98.9410	1.7362	2.7206
	LRaSMD-BA-KTCIMF	1.0000	0.9963	0.0050	1.9963	0.9950	0.9913	199.2500	1.9913	126.7084
	CDASC-BA-TCIMF	1.0000	0.9738	0.0057	1.9738	0.9943	0.9681	172.1203	1.9681	0.7051
	CDASC-BA-KTCIMF	1.0000	0.9963	0.0050	1.9963	0.9950	0.9912	197.9920	1.9912	115.3024
	OSP [5]	0.6643	0.4175	0.2162	1.0818	0.4480	0.2013	1.9307	0.8655	1.5684
	CEM [7-8]	0.9997	0.7275	0.0112	1.7272	0.9885	0.7163	64.8427	1.7160	1.3834
	TCIMF [10]	0.9997	0.7263	0.0120	1.7259	0.9877	0.7142	60.3537	1.7139	0.5664
	KTCIMF [18]	1.0000	1.0000	0.0050	2.0000	0.9950	0.9950	200.0000	1.9950	47.9064
	SDIA [12]	0.7636	0.6288	0.0582	1.3923	0.7053	0.5705	10.7980	1.3341	0.5823
	OSPTD [14]	1.0000	0.7550	0.0072	1.7550	0.9928	0.7478	104.9766	1.7478	3.0006
	HCEM [21]	1.0000	0.9963	0.0050	1.9963	0.9950	0.9913	199.2500	1.9913	0.5819
	ECEM [22]	1.0000	0.9963	0.0050	1.9963	0.9950	0.9913	199.2500	1.9913	15.6800
p ₄	DS-BA-TCIMF	1.0000	0.8063	0.0091	1.8063	0.9909	0.7971	88.3077	1.7971	3.1312
	DS-BA-KTCIMF	1.0000	0.9950	0.0050	1.9950	0.9950	0.9900	199.0000	1.9900	283.4540
	LRaSMD-BA-TCIMF	1.0000	0.7863	0.0065	1.7863	0.9935	0.7797	120.2293	1.7797	2.7018
	LRaSMD-BA-KTCIMF	1.0000	0.9963	0.0050	1.9963	0.9950	0.9913	199.2500	1.9913	127.6413
	CDASC-BA-TCIMF	1.0000	0.9188	0.0062	1.9188	0.9938	0.9126	148.5391	1.9126	0.6925
	CDASC-BA-KTCIMF	1.0000	0.9963	0.0050	1.9963	0.9950	0.9912	199.1527	1.9912	108.1894
	OSP [5]	0.2280	0.2800	0.4259	0.5080	-0.1978	-0.1459	0.6575	0.0822	1.6673
	CEM [7-8]	0.9998	0.7613	0.0109	1.7611	0.9889	0.7504	69.9222	1.7502	1.4795
	TCIMF [10]	0.9998	0.7600	0.0117	1.7598	0.9881	0.7483	64.7226	1.7481	0.5583
	KTCIMF [18]	1.0000	0.9963	0.0050	1.9963	0.9950	0.9913	199.2500	1.9913	46.1595
	SDIA [12]	0.9998	0.7500	0.0121	1.7498	0.9877	0.7379	61.9000	1.7377	0.5713
	OSPTD [14]	0.9999	0.7263	0.0066	1.7262	0.9933	0.7196	109.5398	1.7196	2.9864
	HCEM [21]	1.0000	0.9738	0.0050	1.9738	0.9950	0.9688	194.7500	1.9688	0.5698
	ECEM [22]	1.0000	0.9963	0.0050	1.9963	0.9950	0.9913	199.2500	1.9913	15.6463

p ₅	DS-BA-TCIMF	1.0000	0.8800	0.0084	1.8800	0.9916	0.8716	104.9231	1.8716	3.1891
	DS-BA-KTCIMF	1.0000	0.9963	0.0050	1.9963	0.9950	0.9913	199.2500	1.9913	285.1055
	LRaSMD-BA-TCIMF	1.0000	0.7588	0.0064	1.7588	0.9936	0.7524	119.3697	1.7524	2.7592
	LRaSMD-BA-KTCIMF	1.0000	0.9963	0.0050	1.9963	0.9950	0.9913	199.2500	1.9913	127.9219
	CDASC-BA-TCIMF	1.0000	0.9838	0.0053	1.9838	0.9947	0.9784	185.3363	1.9784	0.7475
	CDASC-BA-KTCIMF	1.0000	0.9938	0.0050	1.9938	0.9950	0.9887	196.9213	1.9887	107.5967
	OSP [5]	0.5176	0.4425	0.4231	0.9601	0.0945	0.0194	1.0458	0.5370	1.8137
	CEM [7-8]	0.9998	0.6863	0.0109	1.6860	0.9889	0.6754	63.0333	1.6751	1.6297
	TCIMF [10]	0.9998	0.6838	0.0116	1.6835	0.9882	0.6722	59.1023	1.6719	0.6122
	KTCIMF [18]	1.0000	1.0000	0.0050	2.0000	0.9950	0.9950	200.0000	1.9950	45.0478
	SDIA [12]	0.7634	0.6288	0.0600	1.3922	0.7035	0.5688	10.4873	1.3322	0.6242
	OSPTD [14]	1.0000	0.6938	0.0058	1.6938	0.9942	0.6879	119.4289	1.6879	3.0557
	HCEM [21]	1.0000	0.9663	0.0050	1.9613	0.9950	0.9613	193.2500	1.9613	0.6214
	ECEM [22]	1.0000	0.9963	0.0050	1.9963	0.9950	0.9913	199.2500	1.9913	15.8237

It is worth noting from Table III that using the joint matrix of $\mathbf{L}+\mathbf{S}$ and kernels instead of the original data to reduce the influences of noise did improve the panel detection performance dramatically. This can be seen that BA-KTCIMF and BA-TCIMF achieved very high AUC_{SNPR} , specifically BA-KTCIMF. In addition, Table III also demonstrated one important fact that relying on $AUC_{(D,F)}$ is not reliable. For example, according to Table III, both CEM and TCIMF achieved $AUC_{(D,F)} = 0.9997$ and 0.9998 compared to BA-TCIMF and BA-KTCIMF which achieved $AUC_{(D,F)} = 1.000$. The differences between these detectors were within an error range, 2×10^{-4} . With such tiny numerical error tolerance, how can we claim that one is better than another. The 3D ROC curve-derived detection measures provide such solutions.

B. San Diego Airport Data Experiments

Similar experiments conducted for the HYDICE 15-panel scene were performed for the San Diego airport data scene. Fig. 7 shows the detection maps produced by OSP, CEM,

SDIA, TCIMF, KTCIMF, OSPTD, DS-BA-TCIMF/KTCIMF, LRaSMD-BA-TCIMF/KTCIMF, HCEM and ECEM. In analogy with the HYDICE data, the visual inspection of Fig. 7 showed the best results which were produced by KTCIMF, various versions of BA-KTCIMF, HCEM and ECEM, all of which had very clean BKG suppression. To further conduct quantitative analysis, Fig. 8 plots 3D ROC curves calculated from the detection maps in Fig. 7 along with their corresponding 2D ROC curves. Table IV tabulates values of $AUC_{(D,F)}$, $AUC_{(D,T)}$, $AUC_{(F,T)}$, AUC_{TD} , AUC_{BS} , AUC_{TDBS} , AUC_{SNPR} , AUC_{ODP} with best in bold, second-best in bold red and third-best in bold blue where the best results also confirmed by visual assessment of Fig. 7. Once again, according to Table IV, all kernel-based target detectors, i.e., three versions of BA-KTCIMF, KTCIMF, HCEM, performed very well and they were among the three best results. For target detectors without using kernels, ECEM was the best.

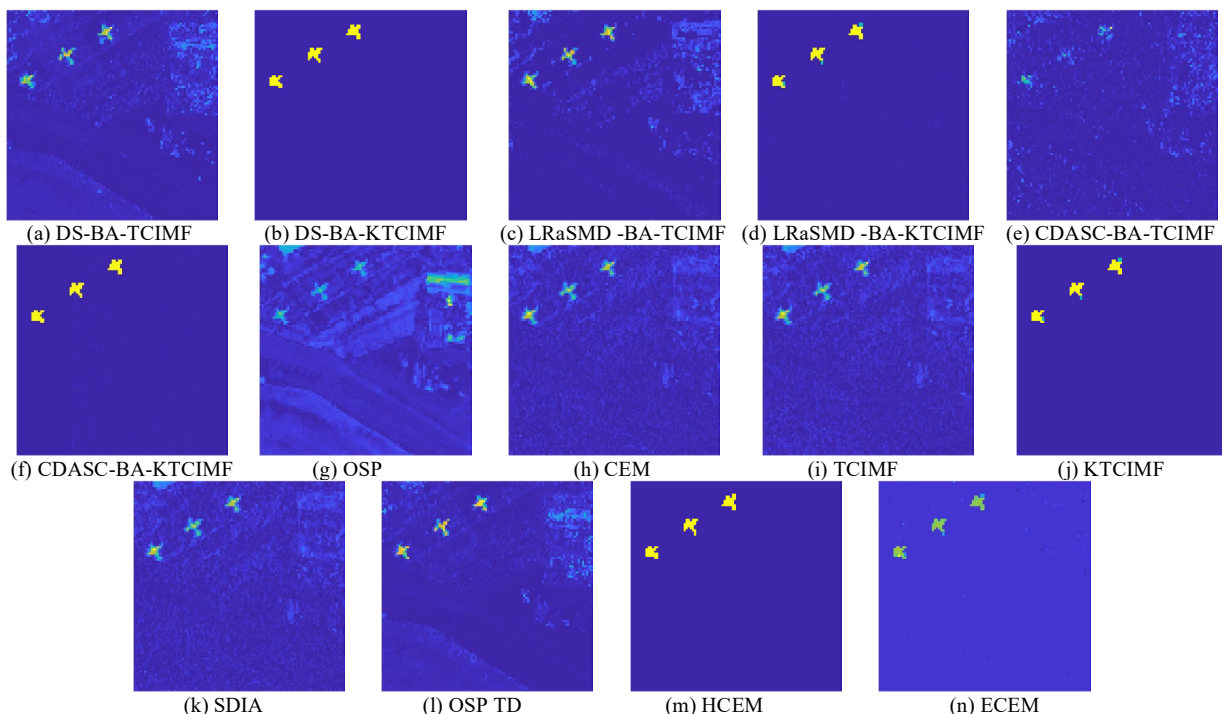


Fig. 7. target abundance detection maps of various target detectors for San Diego data scene

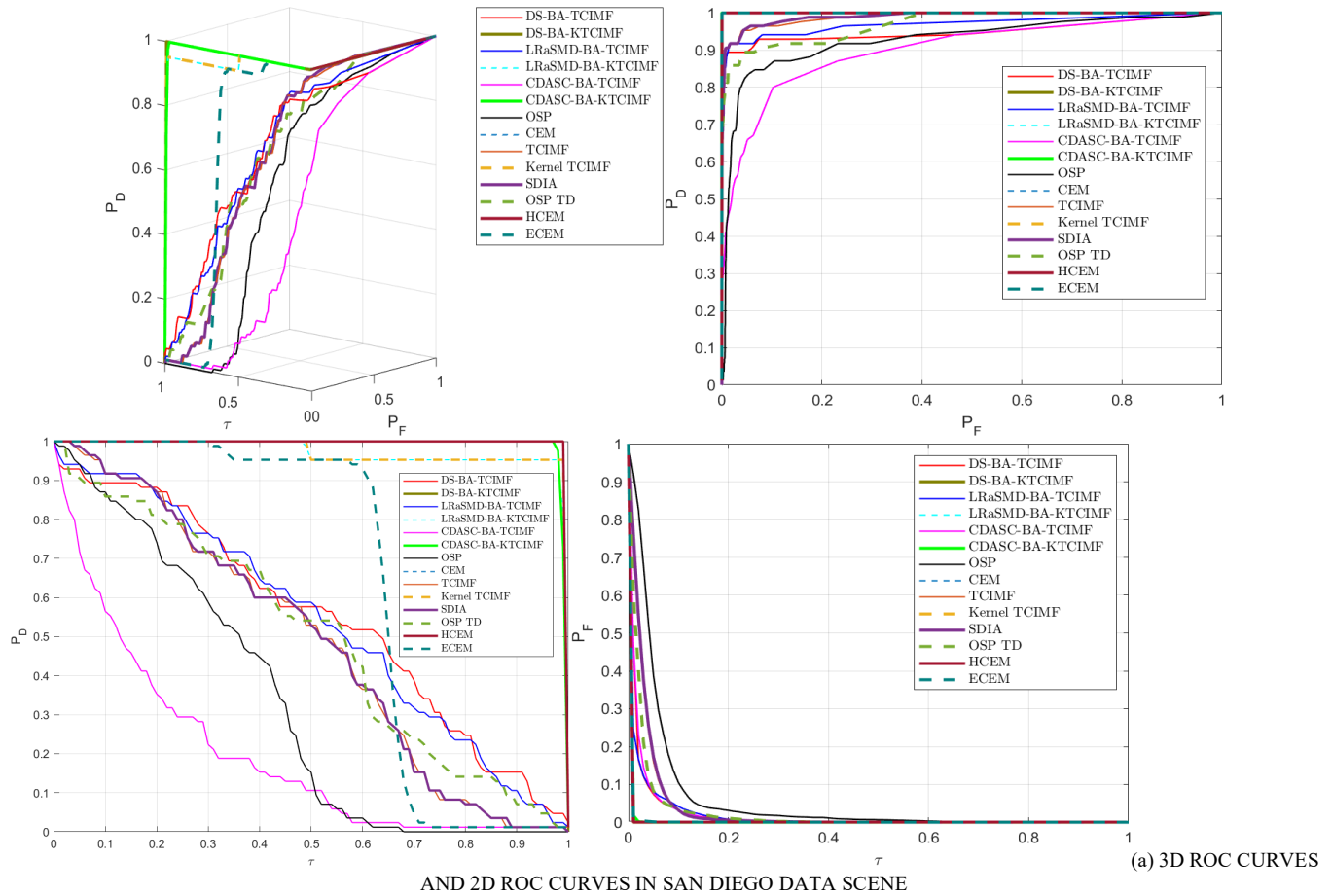


Fig. 8. ROC curves generated from the results in Fig. 7 for San Diego data scene

TABLE IV

AUC VALUES CALCULATED FROM THE THREE 2D ROC CURVES FOR SAN DIEGO DETECTION RESULTS

detector	AUC _(D,F)	AUC _(D,T)	AUC _(F,T)	AUC _{TD}	AUC _{BS}	AUC _{TDBS}	AUC _{SNPR}	AUC _{ODP}	Time(s)
DS-BA-TCIMF	0.9526	0.5486	0.0183	1.5012	0.9343	0.5303	30.0436	1.4829	9.0906
DS-BA-KTCIMF	1.0000	0.9951	0.0050	1.9951	0.9950	0.9901	199.0118	1.9901	3298.9927
LRA-SMD-BA-TCIMF	0.9637	0.5758	0.0158	1.5394	0.9479	0.5600	36.4111	1.5236	8.4569
LRA-SMD-BA-KTCIMF	1.0000	0.9717	0.0052	1.9717	0.9948	0.9665	186.0474	1.9665	1420.5184
CDASC-BA-TCIMF	0.9016	0.1949	0.0193	1.0966	0.8824	0.1757	10.1183	1.0773	1.6254
CDASC-BA-KTCIMF	1.0000	0.9921	0.0052	1.9921	0.9948	0.9869	190.9511	1.9869	1407.2919
OSP [5]	0.9248	0.4036	0.0681	1.3284	0.8567	0.3355	5.9278	1.2603	8.5540
CEM [7-8]	0.9893	0.4819	0.0302	1.4711	0.9590	0.4517	15.9419	1.4409	1.1488
TCIMF [10]	0.9877	0.4871	0.0314	1.4748	0.9563	0.4557	15.5122	1.4434	8.0651
KTCIMF [18]	1.0000	0.9715	0.0052	1.9715	0.9948	0.9663	186.9160	1.9663	602.8169
SDIA [12]	0.9903	0.4826	0.0310	1.4729	0.9593	0.4517	15.5738	1.4419	1.2361
OSPTD [14]	0.9687	0.5656	0.0235	1.5342	0.9452	0.5421	24.1180	1.5108	298.2633
HCEM [21]	0.9998	0.9951	0.0054	1.9949	0.9944	0.9897	184.2908	1.9895	6.8343
ECEM [22]	1.0000	0.6407	0.0054	1.6407	0.9946	0.6353	118.5297	1.6353	48.4120

VI. TRAINING SAMPLING -BASED TCIMF

The experiments conducted in Sections V.A and V.B assumed that the target signatures are provided by prior knowledge or ground truth. In practical applications, this assumption may not be realistic. However, it is known that OSP, CEM, KTCIMF are very sensitive to their used target knowledge. So, this section investigates this issue using training samples instead of complete ground truth to calculate target signatures. Since the HYDICE panel data set has only

19 R panel pixels which are too small to be used as a training sample pool. In this case, the San Diego data set in Fig. 4 was used for this purpose where training samples were randomly selected from the 85 pixels of airplanes to calculate the desired airplane signatures. Two scenarios were considered, 20% random sampling and 5% random sampling from the 85 pixels. Figs. 9 and 10 show the anomaly abundance detection maps of DS-BA-TCIMF, DS-BA-KTCIMF, LRA-SMD-BA-TCIMF, LRA-SMD-BA-KTCIMF, CDASC-TCIMF, CDASC-KTCIMF, OSP, CEM, ICIMF, KTCIMF, SDIA, OSPTD, HCEM and

ECM using 20% and 5% randomly selected training samples respectively. It is very interesting to note that except OSP, CEM, TCIMF which were not affected much by training samples all other target detectors which are performed very well in Fig. 7, have been largely impacted by the use of training samples with their detection performance significantly degraded as the number of training samples is decreased. Figs. 11-12 also plot the 3D ROC curves generated from the results in Figs. 9-10 along with their corresponding three 2D ROC curves. Tables V and VI tabulate the AUC values of 8 detection measures presented in Section IV.C for quantitative studies and analysis with best in bold, second-best in bold red and third-best in bold blue where KTCIMF suffered from exceedingly high computational complexity with very poor performance, while CEM, TCIMF and OSP remains very

effective with very low computational complexity. More interestingly, various versions of BA-TCIMF were still competitive when 20% training samples were used but lost their compactivity when only 5% training samples were used. What is worse is that HCEM and ECM performed very poorly as long as training samples were used instead of the complete ground truth. These experiments were very crucial because they showed that when the sufficient ground truth is necessary for HCEM, ECM, KTCIMF and DS-BA-TCIMF and LRaSMD-TCIMF and CDASC-TCIMF to perform well as documented in Tables III and IV. By contrast, when target signatures are calculated by training samples, their performances are degraded drastically and eventually lose their competency if the training sample size becomes small.

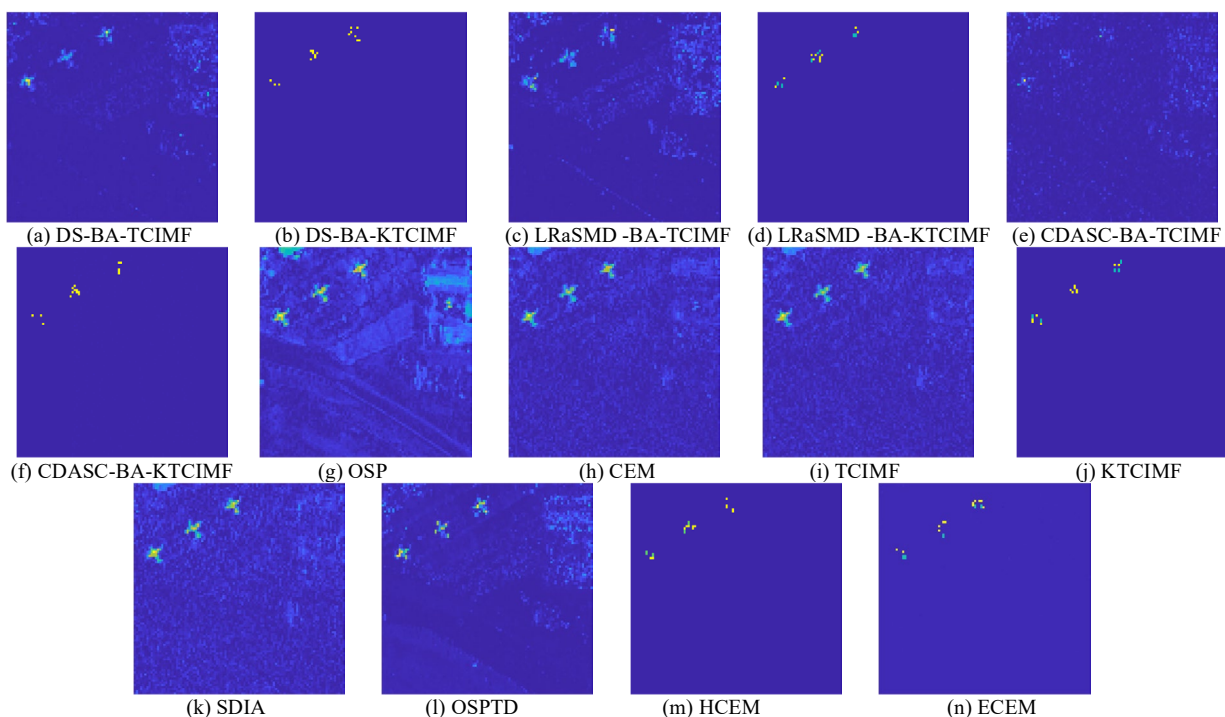
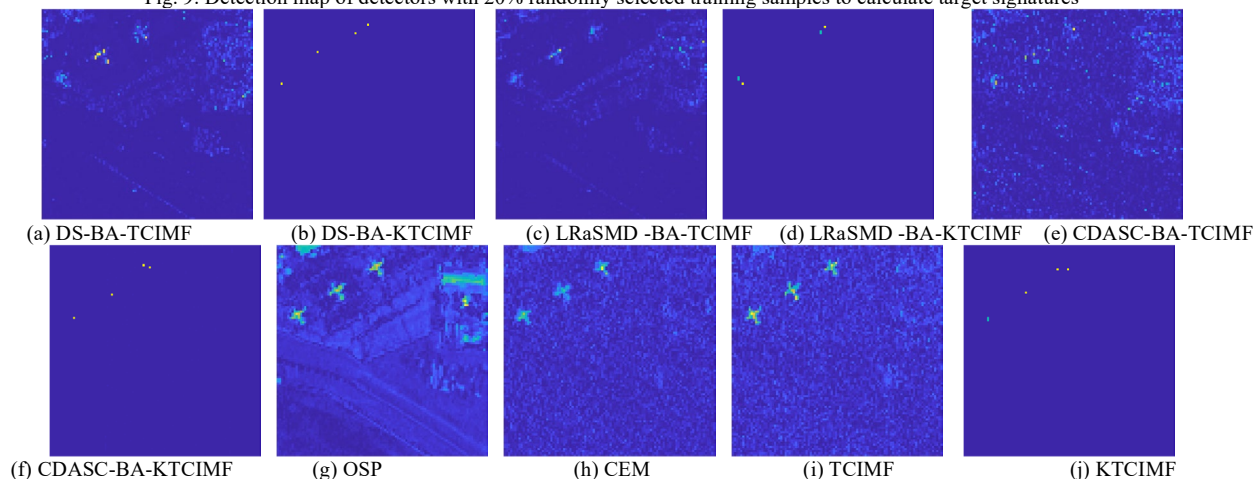


Fig. 9. Detection map of detectors with 20% randomly selected training samples to calculate target signatures



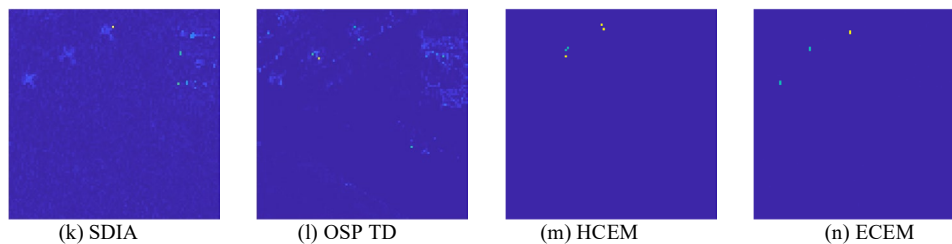
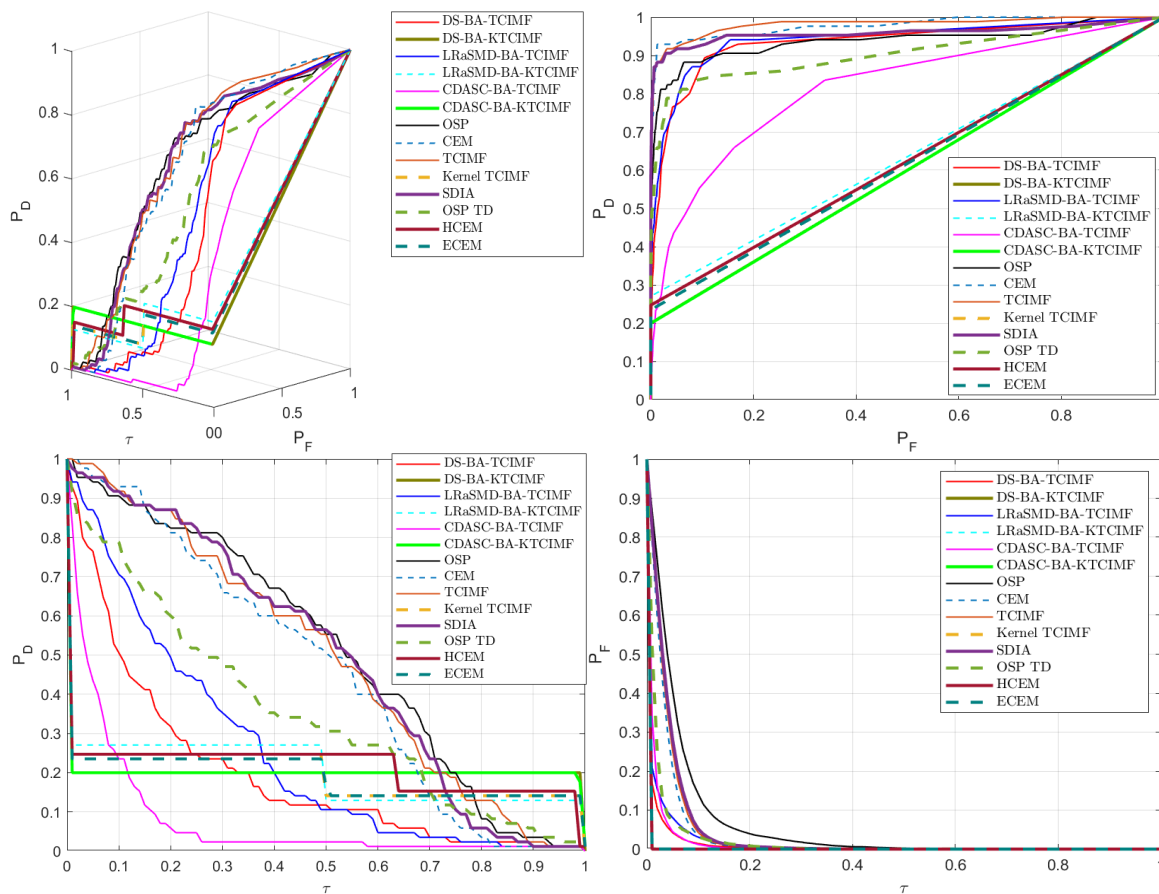
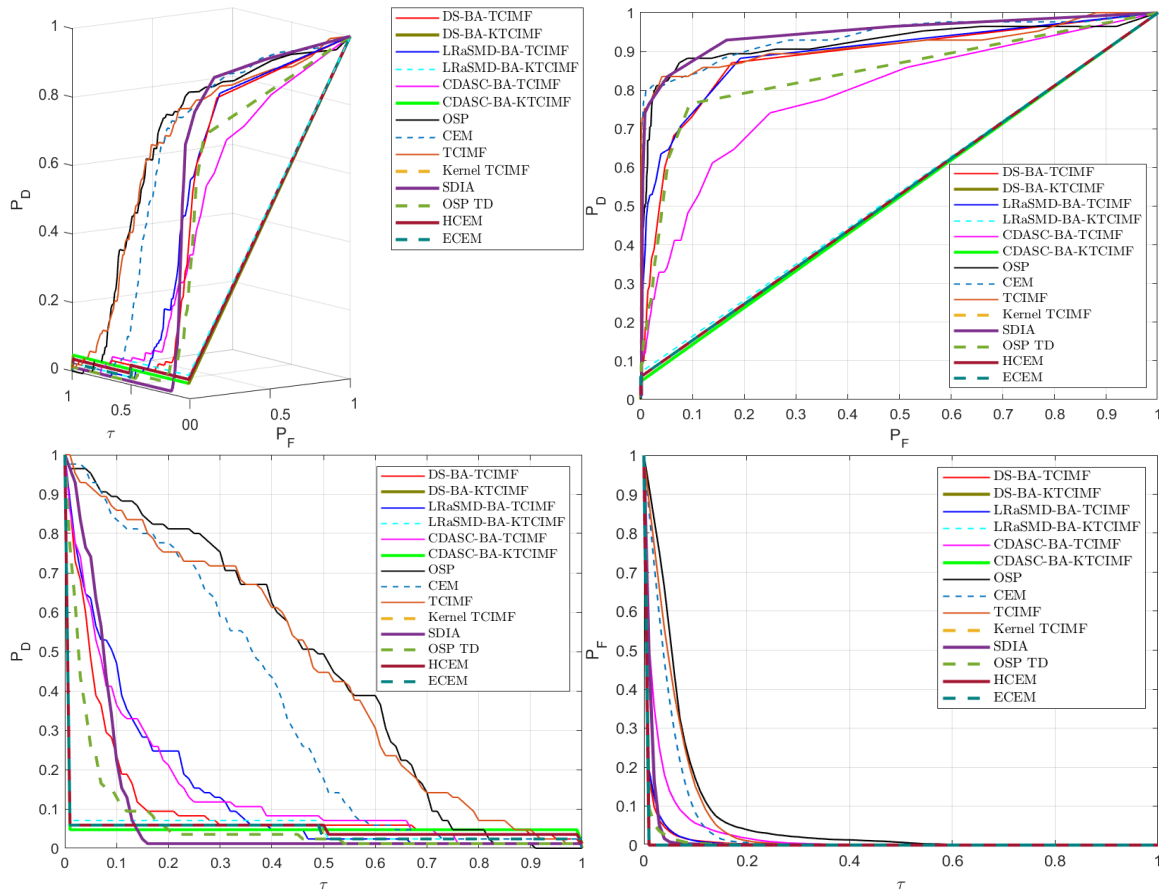


Fig. 10. Detection map of detectors with sampling 5% randomly selected training samples to calculate target signatures



(a) 3D ROC CURVES AND 2D ROC CURVES IN SAN DIEGO DATA SCENE WITH 20% SMAPING RATE

Fig. 11. 3D ROC curve of detectors



(a) 3D ROC CURVES AND 2D ROC CURVES IN SAN DIEGO DATA SCENE WITH 5% SMAPING RATE
Fig. 12. 3D ROC curve of detectors

TABLE V

AUC VALUES CALCULATED FROM THE THREE 2D ROC CURVES IN FIG. 10 FOR SAN DIEGO DETECTION RESULTS

detector	AUC _(D,F)	AUC _(D,τ)	AUC _(F,τ)	AUC _{TD}	AUC _{BS}	AUC _{TDBS}	AUC _{SNPR}	AUC _{ODP}	Time(s)
DS-BA-TCIMF	0.8846	0.1096	0.0111	0.9942	0.8735	0.0985	9.8163	0.9831	9.0423
DS-BA-KTCIMF	0.6000	0.2030	0.0050	0.8030	0.5950	0.1980	40.6000	0.7980	5550.7583
LRaSMD-BA-TCIMF	0.9425	0.2501	0.0159	1.1926	0.9266	0.2342	15.7171	1.1767	9.7393
LRaSMD-BA-KTCIMF	0.6353	0.2024	0.0050	0.8376	0.6303	0.1974	40.4706	0.8326	1465.1743
CDASC-BA-TCIMF	0.9016	0.1949	0.0193	1.0966	0.8824	0.1757	10.1183	1.0773	1.5532
CDASC-BA-KTCIMF	0.5997	0.2028	0.0050	0.8025	0.5947	0.1978	40.4994	0.7975	1436.5258
OSP [5]	0.9391	0.5092	0.0583	1.4483	0.8808	0.4509	8.7327	1.3900	9.0111
CEM [7-8]	0.9779	0.4589	0.0340	1.4369	0.9439	0.4249	13.4973	1.4029	1.0337
TCIMF [10]	0.9550	0.4906	0.0552	1.4456	0.8999	0.4354	8.8900	1.3904	5.2571
KTCIMF [18]	0.6235	0.1966	0.0050	0.8201	0.6184	0.1916	38.9445	0.8151	608.4449
SDIA [12]	0.9586	0.4931	0.0396	1.4517	0.9191	0.4535	12.4649	1.4121	1.3202
OSPTD [14]	0.9035	0.3518	0.0200	1.2553	0.8836	0.3319	17.6343	1.2354	301.3799
HCEM [21]	0.6235	0.2144	0.0050	0.8379	0.6185	0.2094	42.8706	0.8329	2.7533
ECEM [22]	0.6232	0.1910	0.0051	0.8142	0.6181	0.1859	37.4077	0.8091	49.4729

TABLE VI

AUC VALUES CALCULATED FROM THE THREE 2D ROC CURVES IN FIG. 11 FOR SAN DIEGO DETECTION RESULTS

detector	AUC _(D,F)	AUC _(D,τ)	AUC _(F,τ)	AUC _{TD}	AUC _{BS}	AUC _{TDBS}	AUC _{SNPR}	AUC _{ODP}	Time(s)
DS-BA-TCIMF	0.5914	0.1141	0.0507	0.7055	0.5406	0.0634	2.2492	0.6547	8.8871
DS-BA-KTCIMF	0.5235	0.0924	0.0500	0.6159	0.4735	0.0424	1.8471	0.5659	5550.7583
LRaSMD-BA-TCIMF	0.7307	0.1482	0.0515	0.8789	0.6792	0.0967	2.8782	0.8274	9.7393
LRaSMD-BA-KTCIMF	0.5353	0.0929	0.0500	0.6282	0.4853	0.0429	1.8588	0.5782	1465.1743
CDASC-BA-TCIMF	0.6577	0.1494	0.0580	0.8071	0.5997	0.0914	2.5748	0.7491	1.5532
CDASC-BA-KTCIMF	0.5235	0.0929	0.0500	0.6165	0.4735	0.0429	1.8588	0.5665	1436.5258
OSP [5]	0.9232	0.4665	0.0755	1.3897	0.8477	0.3910	6.1779	1.3142	9.0111
CEM [7-8]	0.9073	0.3453	0.0591	1.2526	0.8483	0.2862	5.8448	1.1936	1.0337
TCIMF [10]	0.9096	0.4459	0.0666	1.3555	0.8430	0.3793	6.6968	1.2889	5.2571

KTCIMF [18]	0.5294	0.0918	0.0500	0.6212	0.4794	0.0418	1.8353	0.5712	608.4449
SDIA [12]	0.6103	0.0824	0.0505	0.6927	0.5598	0.0318	1.6303	0.6422	1.3202
OSPTD [14]	0.5625	0.0824	0.0506	0.6449	0.5119	0.0317	1.6270	0.5942	301.3799
HCEM [21]	0.5294	0.0941	0.0500	0.6235	0.4794	0.0441	1.8824	0.5735	2.7533
ECEM [22]	0.5294	0.0865	0.0500	0.6158	0.4793	0.0364	1.7280	0.5658	54.1746

Three remarks are noteworthy.

1. Despite the fact that KTCIMF perform the best in Figs. 5-8 and Tables III and IV, its slight improvement over BA-TCIMF and extremely high computational complexity prevent it from being applicable to practical applications. This is particularly worse when insufficient training samples are used to calculate the desired target signatures as demonstrated in Figs. 9-12 and Tables V and VI. Accordingly, the advantages offered by KTCIMF are diminished.
2. TCIMF is a “pixel-based” target detection technique and does not use windows or machine/deep learning techniques to learn BKG. So, its applicability is not limited by data set size. So, its effective performance has little do with increasing data sets but rather BKG. It is exactly the key idea of BA-TCIMF which introduces two types of BKG annihilation.
3. Lat but not least, deep learning (DL)-based target detection algorithms are not applicable to comparing BA-TCIMF is because BA-TCIMF does not require training samples, while DL does. Comparing BA-TCIMF to DL-based target detection is like comparing apples to oranges. In particular, when DL-based methods are used, they generally use training samples to learn the background. By contrast, BA-TCIMF does not need to do so. Instead, it makes use of BA to accomplish BKG suppression. This is generally more effective than using DL-based methods to estimate BKG for removal. Specifically, the great advantage of BA-TCIMF over the DL-based methods is that BA-TCIMF makes use of data sphering and unsupervised MXSVD to find unwanted BKG signatures through GoDec model. This has been shown by the experiments conducted for the San Diego airport scene in Section VIII in [38] where hCEM and ECEM were shown in [20] to outperform machine learning-based methods in BKG suppression such as PTA (prior-based tensor approximation) in [39], LSDM-MoG (low-rank and sparse decomposition with mixture of Gaussians) in [40] and LRR (low rank representation) in [41]

VII. CONCLUSION

Target-constrained interference-minimized filter (TCIMF) is an effective subpixel target detector in many applications. However, its utilization is limited to the requirement of prior knowledge of the undesired target signatures in \mathbf{U} . This paper presents a generalized TCIMF, called BKG-annihilated TCIMF (BA-TCIMF) which can be implemented in a two-stage process with first stage annihilating BKG followed by a second stage enhancing target detectability (TDE) and improving target BKG suppression (TBS). Depending upon how to annihilate BKG in the first stage, three versions of BA-TCIMF, DS-BA-TCIMF, LRA-SMD-BA-TCIMF and CDA-

BA-TCIMF, are derived in three different ways. The main contributions of this paper can be described as follows.

1. It develops BA-TCIMF as a two-stage target detector which includes TCIMF, SDIA and OSP-TD as special cases. Specifically, three versions of BA-TCIMF are derived, that is, DS-BA-TCIMF, LRA-SMD-BA-TCIMF and CDA-TCIMF.
2. At the first stage, BA-TCIMF annihilates BKG prior to target detection. That is, DS-BA-TCIMF takes care of BKG by DS; LRA-SMD-BA-TCIMF removes BKG by the GoDec-produced low rank space \mathbf{L} via P_L^\perp ; CDA-BA-TCIMF nulls out the CDA-generated PC space as BKG space.
3. At the second stage, BA-TCIMF extracts additional unwanted BKG signatures \mathbf{B}_m to augment the undesired target signature matrix \mathbf{U} to \mathbf{UB}_m to improve target detectability.
4. In the meantime, at the second stage, BA-TCIMF further suppresses target BKG by inverting the correlation matrix of BKG-annihilated data, \mathbf{R}_{BA} . DS-BA-TCIMF operates \mathbf{R}_{BA} in the sphered joint $\mathbf{L}+\mathbf{S}$ space, $\hat{\mathbf{L}}+\hat{\mathbf{S}}$, while LRA-SMD-BA-TCIMF operates \mathbf{R}_{BA} in the joint $\mathbf{L}+\mathbf{S}$ space. Different from DS-BA-TCIMF and LRA-SMD-BA-TCIMF, CDA-BA-TCIMF operates \mathbf{R}_{BA} in the joint $\mathbf{PC}+\mathbf{IC}$ component space.
5. Despite that KTCIMF can be also used to extend to BA-KTCIMF to improve the performance of BA-TCIMF, such effort is not worth. This is because BA-TCIMF has already demonstrated to be very effective and BA-KTCIMF may only improve its performance slightly but not much. Most importantly, the computational complexity of using kernels is exceedingly expensive, specifically, kernelizing the correlation matrix \mathbf{R}_{BA} .

As a final comment, many researchers may think that target detection and anomaly detection are similar detection tasks and expect that one can derive the other. As a matter of fact, this is certainly not true. More specifically, target detection is active detection with known target knowledge as opposed to anomaly detection which is passive detection with no prior target knowledge. There are significant differences between target detection and anomaly detection as detailed in [20], [42] and [23]. Consequently, one cannot simply apply target detection to another detection and vice versa.

REFERENCES

- [1] C.-I Chang, *Hyperspectral Imaging: Techniques for Spectral Detection and Classification*, Kluwer Academic/Plenum Publishers, New York, N.Y., 2003.
- [2] C.-I Chang, *Hyperspectral Data Processing: Algorithm Design and Analysis*, Wiley, New Jersey, 2013.
- [3] C.-I Chang, *Real-Time Progressive Hyperspectral Image Processing: Endmember Finding and Anomaly Detection*, Springer, New York, 2016.

- [4] C.-I Chang, *Real-Time Recursive Hyperspectral Sample and Band Processing: Algorithm Architecture and Implementation*, Springer, New York, 2017.
- [5] J.C. Harsanyi and C.-I Chang, "Hyperspectral image classification and dimensionality reduction: an orthogonal subspace projection approach," *IEEE Trans. on Geoscience and Remote Sensing*, vol. 32, no. 4, pp. 779-785, July 1994.
- [6] C.-I Chang, "Orthogonal subspace projection revisited: a comprehensive study and analysis," *IEEE Trans. on Geoscience and Remote Sensing*, vol. 43, no. 3, pp. 502-518, March 2005.
- [7] J.C. Harsanyi, *Detection and Classification of Subpixel Spectral Signatures in Hyperspectral Image Sequences*, Department of Electrical Engineering, University of Maryland, Baltimore County, MD, 1993.
- [8] W.H. Farrand and J.C. Harsanyi, "Mapping the distribution of mine tailings in the Coeur d'Alene River Valley, Idaho, through the use of a constrained energy minimization technique," *Remote Sens. Environ.* vol. 59, pp. 64-76, 1997.
- [9] C.-I Chang, "Target signature-constrained mixed pixel classification for hyperspectral imagery," *IEEE Trans. on Geoscience and Remote Sensing*, vol. 40, no. 5, pp. 1065-1081, May 2002.
- [10] H. Ren and C.-I Chang, "Target-constrained interference-minimized approach to subpixel target detection for hyperspectral images," *Optical Engineering*, vol. 39, no. 12, pp. 3138-3145, 2000.
- [11] <https://www.harrisgeospatial.com/docs/tdselectmethods.html>.
- [12] Q. Du and C.-I Chang, "A signal-decomposed and interference-annihilated approach to hyperspectral target detection," *IEEE Trans. on Geoscience and Remote Sensing* vol. 42, no. 4, pp. 892-906, April 2004.
- [13] H. Ren and C.-I Chang, "Automatic spectral target recognition in hyperspectral imagery," *IEEE Trans. on Aerospace and Electronic Systems*, vol. 39, no. 4, pp. 1232-1249, October 2003.
- [14] C.-I Chang and J. Chen, "OSP using data sphering and low-rank and sparse matrix decomposition for hyperspectral target detection," *IEEE Trans. on Geoscience and Remote Sensing*, Vol. 59, no. 10, pp. 8704-8722, October 2021.
- [15] C.-I Chang and J. Chen, "Hyperspectral anomaly detection by data sphering and sparsity density peaks," *IEEE Trans. on Geoscience and Remote Sensing*, vol. 60, 5526321, pp. 1-21, 2022.
- [16] T. Zhou and D. Tao, "GoDec: randomized low-rank & sparsity matrix decomposition in noisy case," *Proceedings of the 28th International Conference on Machine Learning*, Bellevue, WA, USA, 2011.
- [17] S. Chen, C.-I Chang and X. Li, "Component decomposition analysis for hyperspectral target detection," *IEEE Trans. on Geoscience and Remote Sensing*, vol. 60, 5516222, pp. 1-22, 2022.
- [18] T. Wang, B. Du and L. Zhang, "A kernel-based target-constrained interference-minimized filter for hyperspectral sub-pixel target detection," *IEEE Journal of Selected Topics in Signal Processing*, vol. 6, no. 2, pp. 626-637, April 2013.
- [19] C.-I Chang, "An effective evaluation tool for hyperspectral target detection: 3D receiver operating characteristic analysis," *IEEE Trans. on Geoscience and Remote Sensing*, vol. 59, no. 6, pp. 5131-5153, June 2021.
- [20] C.-I Chang, "Hyperspectral target detection: hypothesis testing, signal-to-noise ratio and spectral angle theories," *IEEE Trans. on Geoscience and Remote Sensing*, vol. 60, 5505223, pp. 1-23, 2022.
- [21] Z. Zou and Z. Shi, "Hierarchical suppression method for hyperspectral target detection," *IEEE Trans. Geosci. Remote Sens.*, vol. 54, no. 1, pp. 330-342, Jan. 2016
- [22] R. Zhao, Z. Shi, Z. Zou and Z. Zhang, "Ensemble-based cascaded constrained energy minimization for hyperspectral target detection," *Remote Sens.* 2019, 11, 1310; doi:10.3390/rs1111131.
- [23] C.-I Chang, "Constrained energy minimization anomaly detection for hyperspectral imagery," *IEEE Trans. on Geoscience and Remote Sensing*, vol. 60, pp. 1-19, 5517119, 2022.
- [24] X. Jiao and C.-I Chang, "Kernel-based constrained energy minimization (KCEM)," *SPIE Conference on Algorithms and Technologies for Multispectral, Hyperspectral, and Ultraspectral Imagery XIV*, March 16-20, Orlando, Florida, 2008.
- [25] I.S. Reed and X. Yu, "Adaptive multiple-band CFAR detection of an optical pattern with unknown spectral distribution," *IEEE Trans. Acoust. Speech Signal Process.*, vol. 38, no. 10, pp. 1760-1770, Oct. 1990.
- [26] H.V. Poor, *An Introduction to Signal Detection and Estimation*. 2nd ed., New York: Springer-Verlag, 1991.
- [27] E. J. Candès, X. Li, Y. Ma, and J. Wright, "Robust principal component analysis?," *Journal of the ACM*, vol. 58, no. 3, pp. 1027-1063, 2009.
- [28] N. Vaswani, et al. "Robust subspace learning: robust PCA, robust subspace tracking and robust subspace recovery," *IEEE Signal Processing Magazine*, vol. 35, no. 4, pp. 32-55, July 2018.
- [29] N. Vaswani, et al., Special Issue on "Rethinking PCA for modern datasets: theory, algorithms, and applications," *Proc. IEEE*, vol. 106, no. 8, pp. 1274-2716, August 2018.
- [30] C.-I Chang, H. Cao, S. Chen, X. Shang, M. Song and C. Yu, "Orthogonal subspace projection-based GoDec for low rank and sparsity matrix decomposition for hyperspectral anomaly detection," *IEEE Trans. on Geoscience and Remote Sensing*, vol. 59, no. 3, pp. 2403-2429, 2021.
- [31] N. Halko, P. G. Martinsson, and J. A. Tropp, "Finding structure with randomness: probabilistic algorithms for constructing approximate matrix decompositions," *SIAM Rev.*, vol. 53, no. 2, pp. 217-288, 2011.
- [32] C.-I Chang and Q. Du, "Estimation of number of spectrally distinct spectral signal sources in hyperspectral imagery," *IEEE Trans. on Geoscience and Remote Sensing*, vol. 42, pp. 608-619, March 2004.
- [33] C.-I Chang, "Virtual dimensionality for hyperspectral imagery," 28 September 2009, SPIE Newsroom. [DOI: 10.1117/2.1200909.1749]. <http://newsroom.spie.org/x37123.xml>.
- [34] C.-I Chang, "A review of virtual dimensionality for hyperspectral imagery," *IEEE Journal of Selected Topics in Applied Earth Observation and Remote Sensing*, vol. 11, no. 4, pp. 1285-1305, April 2018.
- [35] C.-I Chang, W. Xiong, H.M. Chen and J.W. Chai, "Maximum orthogonal subspace projection to estimating number of spectral signal sources for hyperspectral images," *IEEE Journal of Selected Topics in Signal Processing*, vol. 5, no. 3, pp. 504-520, June 2011.
- [36] C.-I Chang, W. Xiong and C.H. Wen, "A theory of high order statistics-based virtual dimensionality for hyperspectral imagery," *IEEE Trans. on Geoscience and Remote Sensing*, vol. 52, no. 1, pp. 188-208, January 2014.
- [37] O. Kuybeda, D. Malah and M. Barzohar, "Rank estimation and redundancy reduction of high-dimensional noisy signals with preservation of rare vectors," *IEEE Trans. on Signal Processing*, vol. 55, no. 12, pp. 5579-5592, 2007.
- [38] C.-I Chang, "Effective anomaly space for hyperspectral anomaly detection," *IEEE Trans. on Geoscience and Remote Sensing*, vol. 60, 5526624, pp. 1-24, 2022.
- [39] L. Li, W. Li, Y. Qu, C. Zhao, R. Tao and Q. Du, "Prior-based tensor approximation for anomaly detection in hyperspectral imagery," *IEEE Trans. on Neural Network and Learning Systems*, vol. 33, no. 3, pp. 1037-1050, March 2022.
- [40] L. Li, W. Li, Q. Du and R. Tao, "Low-rank and sparse decomposition with mixture of Gaussian for hyperspectral anomaly detection," *IEEE Trans. on Cybernetics*, vol. 51, no. 9, pp. 4363-4372, Sept. 2021.
- [41] Y. Zhang, B. Du, L. Zhang, and S. Wang, "A low-rank and sparse matrix decomposition-based Mahalanobis distance method for hyperspectral anomaly detection," *IEEE Trans. Geoscience Remote Sens.*, vol. 54, no. 3, pp. 1376-1389, Mar. 2016
- [42] C.-I Chang, "Hyperspectral anomaly detection: a dual theory of hyperspectral target detection," *IEEE Trans. Geoscience Remote Sensing* vol. 60, pp. 1-20, 5511720, 2022.



Jie Chen received the B.S. in computer science and applications from Shaanxi University of Science and Technology, Shaanxi, China, in 2003, and the M.S. in computer technology from University of Chinese Academy of Sciences, Beijing, China in 2015. Since 2018, he is pursuing the Ph.D. degree in electrical engineering at Remote Sensing Signal and Image Processing

Laboratory (RSSIPL), University of Maryland Baltimore County (UMBC), MD, USA.

He was with the Honeywell from 2010-2018 where he was an application and system engineer for software requirement design. His interests include statistical signal processing, digital image processing, machine learning and neural networks, compressive sensing, matrix decomposition, and pattern recognition in hyperspectral image processing.



Chein-I Chang (Life Fellow, IEEE) received the B.S. degree in mathematics from Soochow University in 1973y, Taipei, Taiwan, the M.S. degree in mathematics from the Institute of Mathematics, National Tsing Hua University in 1975, Hsinchu, Taiwan, the M.A. degree in mathematics from the State University of New York at Stony Brook in 1977, Stony Brook, N.Y., USA, both the M.S. and M.S.E.E. degrees from the University of Illinois at Urbana-Champaign in 1982, Urbana, IL, USA and the Ph.D. degree

in electrical engineering from the University of Maryland, College Park, in 1987, MD, USA.

Dr. Chang has been with the University of Maryland, Baltimore County (UMBC) since 1987 where he is a Professor in the Department of Computer Science and Electrical Engineering. Dr. Chang authored four books, *Hyperspectral Imaging: Techniques for Spectral Detection and Classification* published by Kluwer Academic Publishers in 2003 and *Hyperspectral Data Processing: Algorithm Design and Analysis*, John Wiley & Sons, 2013, *Real Time Progressive Hyperspectral Image Processing: Endmember Finding and Anomaly Detection* 2016 by Springer and *Recursive Hyperspectral Sample and Band Processing: Algorithm Architecture and Implementation*, Springer 2017. In addition, he also edited three books, *Recent Advances in Hyperspectral Signal and Image Processing*, 2006, *Hyperspectral Data Exploitation: Theory and Applications*, John Wiley & Sons, 2007, *Advances in Hyperspectral Image Processing Techniques*, Wiley, 2022 and co-edited with A. Plaza a book on *High Performance Computing in Remote Sensing*, CRC Press, 2007. Dr. Chang currently serves as an associate editor for *Remote Sensing* and *IEEE Transactions on Geoscience and Remote Sensing*. His research interests include multispectral/hyperspectral image processing, automatic target recognition, and medical imaging.

Dr. Chang is a Fellow of SPIE. He received a National Research Council Senior Research Associateship Award from 2002 to 2003 sponsored by the U.S. Army Soldier and Biological Chemical Command, Edgewood Chemical and Biological Center, Aberdeen Proving Ground, Maryland.